

UC San Diego

UC San Diego Electronic Theses and Dissertations

Title

Synthesis and investigation of nanostructured particles and membranes for energy-related applications

Permalink

<https://escholarship.org/uc/item/3w56c63q>

Author

Kim, Young Jin

Publication Date

2016

Peer reviewed|Thesis/dissertation

UNIVERSITY OF CALIFORNIA, SAN DIEGO

Synthesis and investigation of nanostructured particles and membranes for energy-
related applications

A dissertation submitted in partial satisfaction of the requirements for the degree
Doctor of Philosophy

in

Materials Science and Engineering

by

Young Jin Kim

Committee in Charge:

Professor Renkun Chen, Chair
Professor Shengqiang Cai
Professor Ratnesh Lal
Professor Ping Liu
Professor Joanna M. McKittrick

2016

Copyright
Young Jin Kim, 2016
All rights reserved.

The dissertation of Young Jin Kim is approved, and it is acceptable in quality and form for publication on microfilm and electronically:

Chair

University of California, San Diego

2016

DEDICATION

Dedicated

to

Bongok Hwang, my godmother

and

Seung-hyun Cha, my brother

EPIGRAPH

When you want something,
all the universe conspires in helping you to achieve it.

Paulo Coelho

TABLE OF CONTENTS

SIGNATURE PAGE	iii
DEDICATION.....	iv
EPIGRAPH	v
TABLE OF CONTENTS	vi
LIST OF FIGURES	ix
LIST OF ABBREVIATIONS.....	xi
ACKNOWLEDGEMENTS.....	xii
VITA.....	xv
ABSTRACT OF THE DISSERTATION	xvi
Chapter 1. Introduction	1
1.1 Evaporative cooling using nanostructured surfaces and membranes	1
1.2 Exchange coupled spring magnet using nanotechnology	5
1.3 Thermochromic smart window using VO ₂ (M) nanoparticles	8
1.4 References	10
Chapter 2. High Heat Flux Evaporation through Nanoporous Membranes	13
2.1 Introduction	13
2.2 Experimental.....	18
2.2.1 Characterization of AAO membrane	18
2.2.2 Prepareing wick sample	19

2.2.3 Experimental setup.....	22
2.3 Results and Discussion	25
2.3.1 Observed heat transfer regimes depend on applied power	25
2.3.2 Comparison between the experimental result and the theoretical value	31
2.4 Conclusion	37
2.5 Acknowledgements	38
2.6 References	39
 Chapter 3. Magnetic core-shell structured MnBi/FeCo exchange spring magnet produced by noble sonic agitation assisted PVD process.....	 43
3.1 Introduction	43
3.2 Experimental method.....	47
3.2.1 Preparing ballmilled MnBi particles	47
3.3 Result and discussion.....	53
3.3.1 Magnetic properties	53
3.3.2 Exchange coupling.....	54
3.3.3 Feasibility of SAA-PVD process.....	57
3.4 Conclusion	59
3.5 References	60
 Chapter 4. Thermochromic Vanadium Oxide Film by Thermal decomposition method	63
4.1 Introduction	63

4.2 Experimental method.....	67
4.2.1 Particle synthesis	67
4.2.2 Tengen doping	67
4.2.3 Characterization of particles	67
4.2.4 Film preparing.....	68
4.2.5 Optical property characterization.....	69
4.3 Result and discussion.....	69
4.3.1 Anaysis on the particles	69
4.3.2 IR modulation performance	74
4.3.3 Controlling transition temperature	74
4.4 Conclusion	77
4.5 References	78
Chapter 5. Conclusions and future works	80
5.1 Summary	80
5.2 Future work	84
5.3 References	86

LIST OF FIGURES

Figure 1.1 Regional variation of evaporation around gas-liquid-solid triple phase contact [7]. (© Elsevier)	1
Figure 1.2 Various wicking structures (a) sintered copper particles [4] (b) porous copper [5] (c) silicon pillars [8] (d) multy-artery [9] (© Elsevier [4, 9] , American Institute of Physics[5] The American Society of Mechanical Engineers [8])	2
Figure 1.3 Heat flux achieved by variety of nano structured surfaces and sintered particles [5] (© American Institute of Physics)	3
Figure 1.4 Development of permanent magnetic materials and (BH) _{max} of each materials [1]. (© John Wiley & Sons, Inc)	5
Figure 1.5 Magnetic properties of (Nd _{0.8} Ce _{0.2}) _{2.4} Fe ₁₂ Co ₂ B depend on temperature (#1-melt-spun ribbons, #2-die upset magnet and #3-die upset magnet) (© John Wiley & Sons, Inc) [3].....	6
Figure 1.6 Suggested designs of exchanged coupled spring magnets [2]. (© The American Physical Society)	6
Figure 1.7 Graphical diagram of the working principle of the thermochromic smart windows or tiles [6]. (© Elsevier).....	9
Figure 2.1 Heat flux inside of nano pores as a function of depth.	14
Figure 2.2 SEM images of AAO membrane (a)After Pt heating layer deposition. (b) Pore boundaries determined by Image J program. (c) An overview of cross section image of the AAO membrane. (d) A closed view of AAO membrane cross section.	18
Figure 2.3 Wick sample preparation detail.	19
Figure 2.4 Experimental set up: (a) Overview of set up schematic. (b) Image of the testing apparatus placed in the vacuum chamber. (c) Image of a wicking sample. (d) SEM image of the AAO membrane.	21
Figure 2.5 Liquid supply channel and electrical wire connection. (a) Schematics of connections. (b) Liquid channel body. (c) After the wick sample is mounted on the liquid channel body (c) After one side of electrical connection-clamp is installed. (d) Electrical wires are clamped (f) overview of the sample assembly.23	23
Figure 2.6 Temperature and resistance calibration curve of the Pt heater.....	24
Figure 2.7 Summarized heat dissipation versus temperature.	25

Figure 2.8 Temperature dynamic at various heating power.	27
Figure 2.9 Images of the membrane surface at various heat dissipating regimes: The images are taken at 250 frames per second (FPS) by FastecImaging IL-5 high-speed camera. The main mode of heat transfer at each of the images is.	30
Figure 2.10 Heat loss through the fixture without liquid supply.	34
Figure 3.1 The concept of the sonic agitation assisted particle sputtering.	47
Figure 3.2 The structure of the Sonic agitation assisted particle sputtering system.	48
Figure 3.3. The photographic image of vacuum feed through manipulator (a and b) The image of the manipulator front and back. (c) The manipulator on the sputtering chamber. (d) the connection between the manipulator and the compartment.	49
Figure 3.4 The image of the particle carrying compartment (a) when the compartment is open. (b) when the compartment is closed. (c) The side image.	51
Figure 3.5. The photograph of the sputtering chamber and ultrasonic vibrating pot. ...	52
Figure 3.6 Image of the MnBi particles	53
Figure 3.7 M-H loop measurement of (a) FeCo particles (b) Ball milled MnBi (black) and After SAPVD process (Red).	55
Figure 4.1 Crystalline structure change of VO ₂ (M) depends on the temperature.	64
Figure 4.2 SEM images of the VO ₂ particles annealed at (a) 500C (b) 450C (c) 400C (d) 350C for 3hours	69
Figure 4.3 XRD pattern of VO ₂ particles annealed at (a) 500 °C (b) 450 °C (c) 400 °C (d) 350 °C	70
Figure 4.4 Image of ball milled particles and particles embedded in polymer matrix .	72
Figure 4.5 XRD patterns of VO ₂ particles with tungsten concentration of (a) 0% (b) 0.5% (c) 1.0% (d) 1.5% (e) 2.0% (f) 2.5%. Peaks JCPDS #00-44-0252 is presented at the bottom.	73
Figure 4.6 Optical measurement of the VO ₂ embedded film at room temperature (blue) at 90 °C (red)	74
Figure 4.7 Change in transiting temperature depends on percentage of tungsten doping (a) DSC curves of VO ₂ particles with different W concentration (b) linear fitting of transition temperature change.	75

LIST OF ABBREVIATIONS

AAO, anodized aluminum oxide

SAA-PVD, sonic agitation assisted physical vapor deposition (jumping sputtering)

$(BH)_{\max}$, maximum energy product

RE, rare earth

H, external magnetic field

H_c, coercive force

EDX, energy-dispersive x-ray spectroscopy

LTP-MnBi, low-temperature phase manganese bismuth

M_r, remnant magnetization

M_s, saturation magnetization

SEM, scanning electron microscopy

TEM, transmission electron microscopy

VSM, vibrating sample magnetometry

XRD, x-ray diffraction

VO₂ (M), vanadium dioxide monoclinic phase

IR, infra read

PVP, Polyvinylpyrrolidone

PET, Polyethylene terephthalate

ACKNOWLEDGEMENTS

I was very lucky to have great advisers while I was studying at UCSD. My former adviser Prof. Sungho Jin always inspired me with his noble ideas. I wished his health was better so that I could get his advising longer time. My former co-adviser Prof. Ami Berkowitz taught great enthusiasm about research. It is my great sorrow that my loving adviser is no longer living in this world. Prof. Joanna McKittrick gave me an opportunity that changed my entire course of life. I was able to discover my talent and my real passion in research while I was working in her lab as an undergrad assistant. My current adviser Professor Renkun Chen changed the direction of my attention towards to the theoretical aspect of research and scientific reasoning. I appreciated that he helped me become a scientist who eager to learn more of fundamental knowledge which will be essential for the rest of research in my life.

I am much honored to have all great professors, who I wished to work together, in my committee. Prof. Renkun Chen, Prof. Shengqiang Cai, Prof Ratnesh Ral, Prof. Ping Liu, and Joanna McKittrick shared their great knowledge with me and gave great advice.

It was a great joy to work with my previous research team members. Dr. Chulmin Choi was a great team leader while I was working in Professor Sungho Jin's group. Dr. Kyung-Jun Hwang was my mentor who taught me many of research skills. Dr. Gunwoo Kim always opened his door for discussions which helped me a lot. Dr. Doyoung Choi shared his research experience with me. Dr. Calvin Gardner inspired me

with his new ideas. I am so glad that we will work together as a team again in a small startup company, which Dr. Chulmin Choi started, to continue our research.

I am grateful to all my project team members. Dr. Phi Nguyen and Dr. Chin-Hung Liu have worked together with me on developing rare earth free magnets. We also have modified and improved ‘Spark Erosion’ machine which is a masterpiece of Prof. Berkowitz. I was joyful to work together with Dr. Phi Nguyen and Dr. Chin-Hung Liu. Qingyang Wang, Kristine McGrath, and David Wooil Jeong have worked together on evaporative cooling. There were many exciting moments during the project. I also appreciate for their hard work.

I also want to acknowledge all my friends and colleagues; Dr. Taekyung Kim, Dr. Soonshin Kwon, Dr. Jaeyun Moon, Dr. Dongwon Chun, Dr. Cihan Kuru, Dr. Cyrus Rustomji, Serdar Yavuz, Jianlin Zheng, Shuang Cui, Sahngki Hong, Sun-mi Shin Xing Xing and Eric Lolan for their helpful discussion and contribution.

Special thanks to my loving English teacher Rose Sleigh who taught me how to write and speak English properly.

Bongok Hwang, my godmother and Seung-hyun Cha, my brother raised me up each time I fell. Without their help and love, I couldn’t finish my study. They also taught me to live my life with smile and confidence.

I wish to express my love to my wife Inae and my son Joshua Shimeen Kim who born while I am writing this dissertation. They are the true joy of my life.

Finally, I wish to thank my parent for their support and encouragement throughout my study. I wish to live my life that they can be proud of me.

Chapter 2, in full is currently being prepared for submission for publication of the material. Young Jin Kim, Qingyang Wang, Kristine McGrath and Renkun Chen “High Heat Flux Evaporation through Nanoporous Membranes” The dissertation author was the primary investigator and author of the paper.

VITA

- 2012 Bachelor of Science, University of California, San Diego
- 2012-2013 Research Assistant, University of California, San Diego
- 2013 Master of Science, University of California, San Diego
- 2013-2016 Research Assistant, University of California, San Diego
- 2014 Teaching Assistant, Department of Mechanical Engineering, University
of California
- 2016 Doctor of Philosophy, University of California, San Diego

ABSTRACT OF THE DISSERTATION

Synthesis and investigation of nanostructured particles and membranes for energy-related applications

By

Young Jin Kim

Doctor of Philosophy in Materials Science and Engineering

University of California, San Diego, 2016

Professor Renkun Chen, Chair

Nanostructured materials exhibit useful properties that are not found in the same materials in bulk form. (1) Dramatically increase surface and area and roughness of nanostructured materials is advantageous for evaporative cooling, which is one of the main subjects in this dissertating, due to the strong capillary effect and high density of gas-liquid-solid triple junctions. (2) In magnetic materials, when the size of the

magnetic material is decreased to submicron or nano size, magnetic coercivity increases since magnetic domains are confined by the size of the material. (3) Also, unique optical properties of materials in nano size can be utilized for thermal managing and energy saving application.

In Chapter 2 of this dissertation, I described the demonstration of using nanoporous membranes in evaporative cooling. Nanoporous membranes have been proposed and theoretically shown as a promising candidate for high heat flux evaporative heat transfer. However, the experimentally demonstrated heat flux has so far been significantly lower than the theoretical prediction, which has cast doubt on the feasibility of achieving a high heat flux from nanoporous membranes. Here we carried out evaporative heat transfer experiments using isopropyl alcohol (IPA) through anodized aluminum oxide (AAO) membranes. For membranes with a 200nm average pore size on a 0.5cm^2 size area, we demonstrated a high evaporative heat flux of $210\text{W}/\text{cm}^2$ based on the overall AAO surface area, or $\sim 400\text{W}/\text{cm}^2$ if only the pore area is considered. This heat flux is close to the theoretical value of $572\text{W}/\text{cm}^2$ (based on the pore area) for IPA evaporation through nanoporous membranes. Using time synchronized high-speed images, it was verified that evaporation was the main heat transfer mode in the high heat flux regime. The demonstration of high heat flux evaporation through nanoporous membranes, close to the theoretical limit and on a relatively large area (0.5cm^2), is significant for the future development of high heat flux thermal management technology for electronic devices.

In chapter 3, I presented a noble technique to achieve exchange coupling of hard phase magnetic materials and soft phase magnetic materials. Exchange coupled spring magnets have been suggested as a possible replacement of rare earth contained strong magnets. We have chosen LPT-MnBi as hard phase and FeCo as soft phase magnetic material, as many early conducted theoretical modeling suggests. The optimal size of hard phase magnet for the exchange coupling (approximately twice of single magnetic domain size, $\sim 2\mu\text{m}$ for MnBi) was achieved by conventional ball milling process, and the shell layer of FeCo was deposited by a noble process called sonic agitation assisted physical vapor deposition (SAA-PVD). TEM image and EDX mapping shows uniform coating of FeCo outer shell layer on the MnBi core. The thickness of the shell layer was in the range of 10~35nm which is slightly less than twice of single domain size of FeCo. Magnetic remanence of ball milled MnBi particles was increased from $M_s = 36$ emu/g to 51 emu/g after SAPVD process while the coercivity was slightly decreased from 1.1T to 1.0T. $(BH)_{\text{max}}$ of the particles after the SAA-PVD process was about 2.5MGOe. Smooth demagnetization curve that resembles that of single magnetic materials and high increase of magnetic remanence suggest that exchange coupling was achieved.

In chapter 4, a new route to synthesize thermochromic VO₂ particles and properties of the film using the particles was presented. A temperature responding fully reversible metal to insulator phase transition (MIT) accompanied by a change of optical properties only found in Vanadium dioxide monoclinic phase (VO₂ (M)) has potential for huge energy saving application by controlling the amount of infrared (IR) light enter into buildings. More synthetic routes are still worthy to be explored because of

difficulty in mass production of VO₂ (M). In this work, we demonstrated a combination of thermal decomposition method subsequent ball milling process to produce pure VO₂ (M) particles. The size of the synthesized particles was between 20 and 200nm. IR modulating smart film was fabricated by blade casting mixture of synthesized VO₂ (M) particles and PVP on PET film. The thickness of the film was about 300nm and particles were uniformly dispersed in the film. Despite the irregular shape of the particles and the fact that few portion of the synthesized particles exceeding suggested optimal size range, the transmittance of little less than 40% and the IR modulation of about 20% which values are practically useful was achieved.

1.1 Evaporative cooling using nanostructured surfaces and membranes

Steady evaporation that utilizes huge latent heat upon phase change of liquid is a desirable mode of heat dissipation and is a phenomenon that is already widely being used in cooling devices such as heat pipes [10]. The performance of these devices can be further improved by employing nano or microstructured surface, sintered particles or membranes because of increased density of gas-liquid-solid triple phase contact [11].

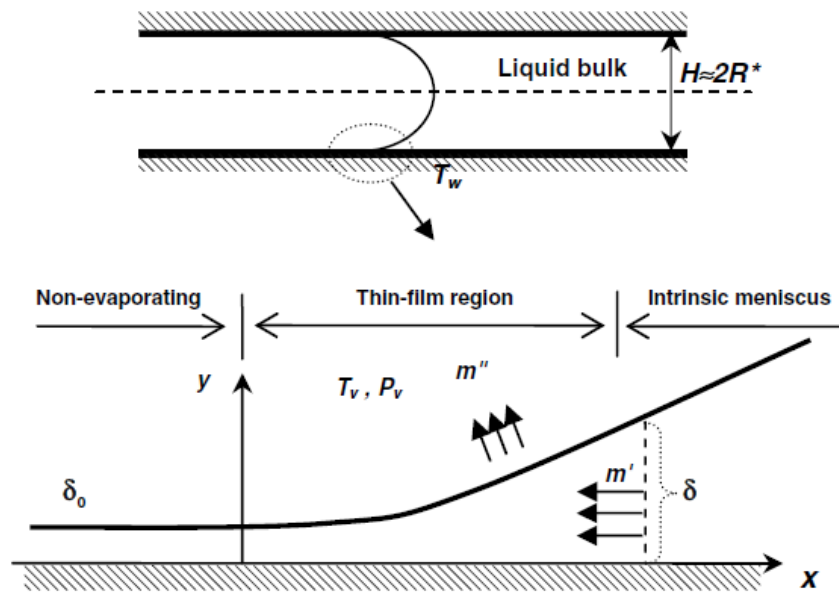


Figure 1.1 Regional variation of evaporation around gas-liquid-solid triple phase contact [7]. (© Elsevier)

To understand how increasing triple phase contact enhances the evaporative heat dissipation, it is necessary to comprehend the fundamental of the evaporation in a meniscus. The schematic diagram of evaporation depend on the region of menisci depicted in Figure 1.1 is a widely accepted theory of evaporation in triple phase contact, and also verified by many researchers by experiment and simulation work [7, 12]. In the non-evaporating region in Figure 1.1 or widely known as an absorbed region, the strong interaction between solid and liquid film that is comprised of only a few layers of molecules prevent evaporation. In the intrinsic meniscus region, due to the thick layer of the liquid, thermal resistance is large therefore heat transfer from the solid to the liquid surface is small, and evaporation is not effective. Evaporation most actively occurs in thin film region. In this region, the interaction of liquid molecules with sold is moderate while thermal resistance is small enough [12].

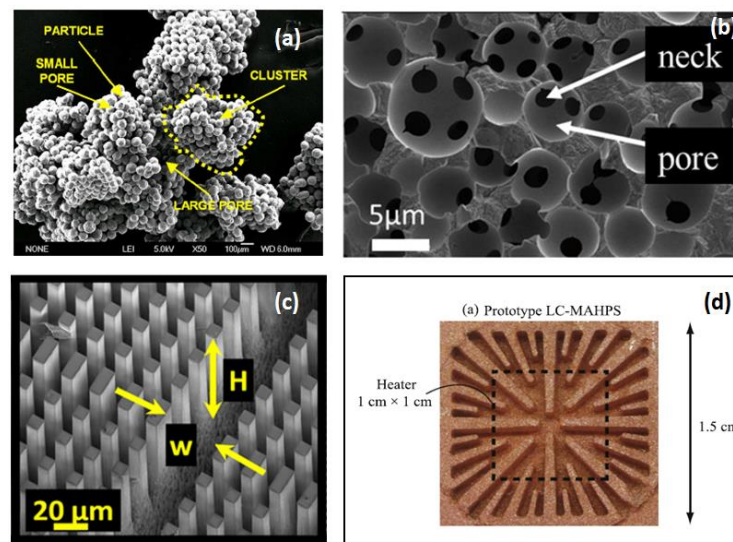


Figure 1.2 Various wicking structures (a) sintered copper particles [4] (b) porous copper [5] (c) silicon pillars [8] (d) multy-artery [9] (© Elsevier [4, 9] , American Institute of Physics[5] The American Society of Mechanical Engineers [8])

Nano or microstructures not only increase the density of the triple phase contact but also provide the huge capillary force. A variety of geometry such as sintered copper particles [4], porous copper [5], silicon pillars [8], multi-artery [9] as shown Figure 1.2 have been explored to achieve high heat flux. Few of these studies reported over $1\text{kW}/\text{cm}^2$ as summarized in Figure 1.3. However, most of them either had high superheat or achieved high heat flux on the very small area (less than 0.1cm^2). In Chapter 2 of this dissertation, I will discuss our demonstration of high heat dissipation using AAO membranes. The significant of our demonstration is that we achieved high heat flux on a relatively large area (0.5cm^2) at under 80°C which is practical operation temperature of many electrical components. The critical heat flux that was achieved is

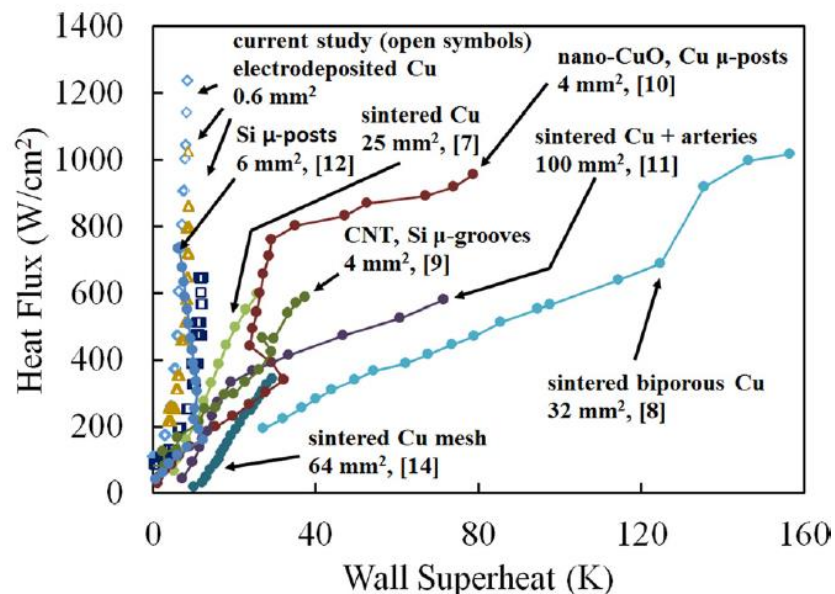


Figure 1.3 Heat flux achieved by variety of nano structured surfaces and sintered particles [5] (© American Institute of Physics)

also close to the theoretical calculation, and further systematic study will be useful information to verify early theoretical works.

1.2 Exchange coupled spring magnet using nanotechnology

Strong permanent magnets are a crucial component of electrical motors and power generators. More than 20% of electricity being generated in the USA is consumed by electrical motors in the industrial sector, and a huge amount of energy could be saved by improving the even small percentage of efficiency of the motors [1]. Moreover, as electrical cars gradually but eventually will replace all fossil fuel based cars, the demand of the strong permanent magnets that are directly related to the performance of the electrical motors are getting increased.

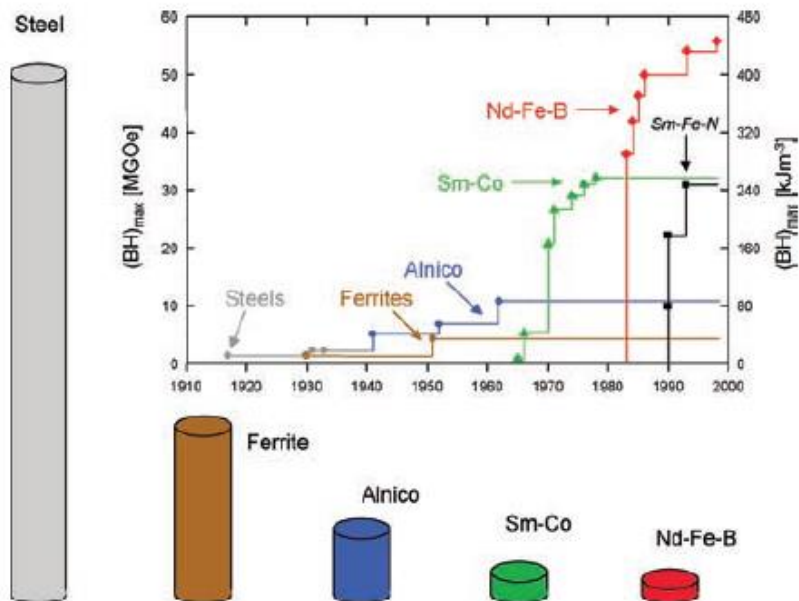


Figure 1.4 Development of permanent magnetic materials and $(BH)_{max}$ of each materials [1]. (© John Wiley & Sons, Inc)

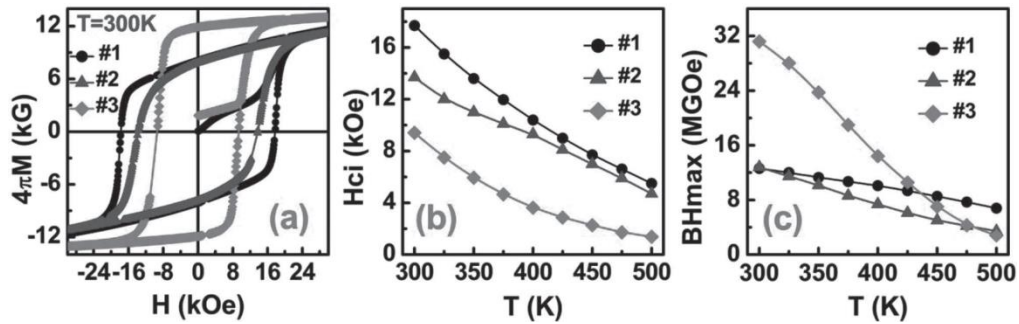


Figure 1.5 Magnetic properties of $(\text{Nd}_{0.8}\text{Ce}_{0.2})_{2.4}\text{Fe}_{12}\text{Co}_2\text{B}$ depend on temperature (#1- melt-spun ribbons, #2-die upset magnet and #3-die upset magnet) (© John Wiley & Sons, Inc) [3]

Currently, sustainability of the permanent magnet highly depends on the supply of Rare earth elements such as Nd, Sm, and Dy [13]. Before the rare earth magnets were discovered, Maximum energy product $(BH)_{max}$ of the strongest permanent magnet was about 5.5MGOe [1, 14]. The highest $(BH)_{max}$ value was dramatically increased to $\sim 56\text{MGOe}$ with the discovery of the $\text{Nd}_2\text{Fe}_{14}\text{B}$. However, the amount of rare earth reserved is limited and the supply may not meet the demand since the number of electrical cars is increasing fast. Another problem of the rear earth magnet is that the coercivity of the NdFeB based magnets decreases dramatically as temperature increases, and at 200°C which is the operation temperature of the most of the motors [15]. In this regard, Development of rare earth free permanent magnet is crucial.

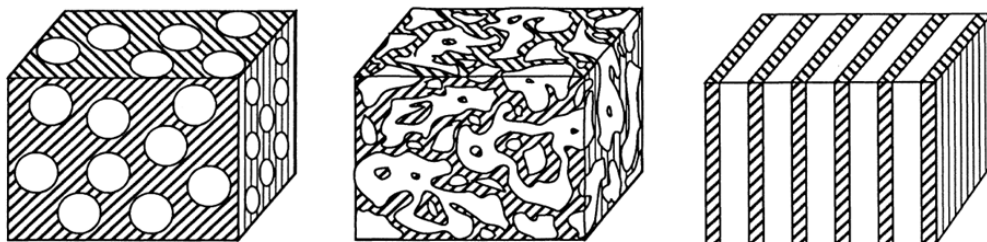


Figure 1.6 Suggested designs of exchanged coupled spring magnets [2]. (© The American Physical Society)

Exchange coupled spring magnet is a design of artificial nanocomposites that create powerful magnets that exhibit energy product $(BH)_{\max}$ as high as rare earth based magnets. In this design, hard phase magnet and soft magnet layers or particles are alternatively arranged, and a strong magnetic reaction occurs at the boundaries. Soft magnets can be highly magnetized but also loose magnetization upon removal of the external magnetic field. In contrast, hard magnets have low magnetic saturation value but once magnetized, it hardly loses the magnetization and changes the direction. In exchange coupled spring magnet, hard phase magnet layer or particles increase the coercivity of soft magnets while soft magnet increase the overall magnetization moment [16]. Figure 1.6 shows the suggested configuration of the exchange coupled spring magnets.

I will discuss our noble approach to realize the exchange coupling spring magnet design using sonic agitation assisted PVD process (SAA-PVD). Previously, most of demonstrations were done by epitaxial growth of the magnetic materials which is slow and expensive. Our approach starts with a large volume of submicron sized particles, therefore, suitable for practical production.

1.3 Thermochromic smart window using VO₂ (M) nanoparticles

Controlling amount of light enters through windows is a great solution to save energy spent on heating and air conditioning. Sunlight light reaches the surface of the earth provides around 600 W/m² of energy in average. In hot weather, blocking sunlight minimizes use of air conditioning, however, blocking sunlight in cold weather causes spending more energy for heating. More than 45% of prime energy is consumed by offices, and residential buildings in most of countries, and heating and cooling is responsible for around 38% of energy use in buildings. Considering \$1.205 trillion of total energy expenditure of U.S.[17], even small percentage of reduction in energy used in buildings could result in saving a huge sum of the money.

Adaptive smart window or tiles using VO₂(M) as shown in Figure 1.7 is an economic and effective solution to control incoming sunlight. VO₂(M) exhibit a fully reversible metal to insulator phase transition. When the surrounding temperature is lower than its transition temperature (T_c~68C), VO₂(M), shows characteristics of semiconductors, and above the T_c, VO₂(M) transit into metal state due to crystalline structure change into VO₂(R) [6]. As VO₂(M) is made into thin (less than ~100 nm) film MIT accompanies the change of optical properties.

Traditionally, pure VO₂(M) films were only produced in high-vacuum processes such as pulsed-laser deposition, molecular beam epitaxial growth, sputtering and CVD [18, 19]. In last decade, smart window films produced by VO₂(M) particles embedded in a polymer matrix has been widely explored, and many of design achieved over 40% of constant visible range light transmittance with 20% of switching IR range light

transmittance. The later approach is more suitable for larger scale production as long as $\text{VO}_2(\text{M})$ particles can be produced in large scale. Currently one of most explored synthetic method, hydrothermal can produce only small amount of particles. Other synthetic methods produce rather large sized particles. Therefore adding one more route to produce pure $\text{VO}_2(\text{M})$ is still worthy. In this dissertation, I will discuss our new approach to produce pure $\text{VO}_2(\text{M})$ particles.

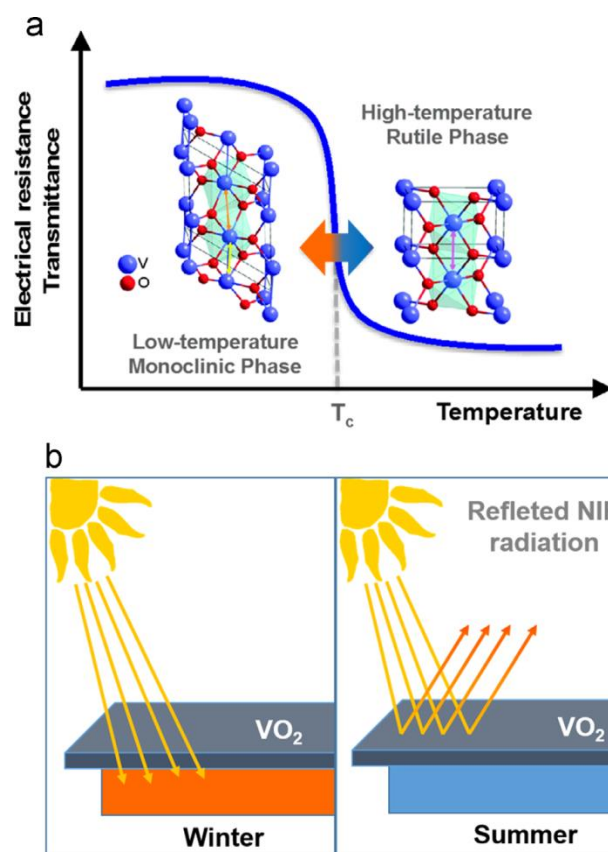


Figure 1.7 Graphical diagram of the working principle of the thermochromic smart windows or tiles [6]. (© Elsevier)

1.4 References

1. Gutfleisch, O., M.A. Willard, E. Brück, C.H. Chen, S. Sankar, and J.P. Liu, *Magnetic materials and devices for the 21st century: stronger, lighter, and more energy efficient*. *Advanced materials*, 2011. **23**(7): p. 821-842.
2. Skomski, R. and J.M.D. Coey, *GIANT ENERGY PRODUCT IN NANOSTRUCTURED 2-PHASE MAGNETS*. *Physical Review B*, 1993. **48**(21): p. 15812-15816.
3. Pathak, A.K., M. Khan, K.A. Gschneidner, R.W. McCallum, L. Zhou, K. Sun, K.W. Dennis, C. Zhou, F.E. Pinkerton, and M.J. Kramer, *Cerium: an unlikely replacement of dysprosium in high performance Nd-Fe-B permanent magnets*. *Advanced Materials*, 2015. **27**(16): p. 2663-2667.
4. Semenic, T. and I. Catton, *Experimental study of biporous wicks for high heat flux applications*. *International Journal of Heat and Mass Transfer*, 2009. **52**(21-22): p. 5113-5121.
5. Palko, J.W., C. Zhang, J.D. Wilbur, T.J. Dusseault, M. Asheghi, K.E. Goodson, and J.G. Santiago, *Approaching the limits of two-phase boiling heat transfer: High heat flux and low superheat*. *Applied Physics Letters*, 2015. **107**(25): p. 253903.
6. Gonçalves, A., J. Resende, A.C. Marques, J.V. Pinto, D. Nunes, A. Marie, R. Goncalves, L. Pereira, R. Martins, and E. Fortunato, *Smart optically active VO₂ nanostructured layers applied in roof-type ceramic tiles for energy efficiency*. *Solar Energy Materials and Solar Cells*, 2016. **150**: p. 1-9.
7. Wang, H., S.V. Garimella, and J.Y. Murthy, *An analytical solution for the total heat transfer in the thin-film region of an evaporating meniscus*. *International Journal of Heat and Mass Transfer*, 2008. **51**(25-26): p. 6317-6322.
8. C'oso, D., V. Srinivasan, M.-C. Lu, J.-Y. Chang, and A. Majumdar, *Enhanced Heat Transfer in Biporous Wicks in the Thin Liquid Film Evaporation and Boiling Regimes*. *Journal of Heat Transfer*, 2012. **134**(10): p. 101501-101501.
9. Hwang, G.S., E. Fleming, B. Carne, S. Sharratt, Y. Nam, P. Dussinger, Y.S. Ju,

- and M. Kaviany, *Multi-artery heat-pipe spreader: Lateral liquid supply*. International Journal of Heat and Mass Transfer, 2011. **54**(11–12): p. 2334-2340.
10. de Bock, H.P.J., S. Chauhan, P. Chamarthy, S.E. Weaver, T. Deng, F.M. Gerner, M.T. Ababneh, and K. Varanasi. *On the Charging and Thermal Characterization of a micro/nano structured Thermal Ground Plane*. in *Thermal and Thermomechanical Phenomena in Electronic Systems (ITherm), 2010 12th IEEE Intersociety Conference on*. 2010. IEEE.
 11. Narayanan, S., A.G. Fedorov, and Y.K. Joshi, *Heat and mass transfer during evaporation of thin liquid films confined by nanoporous membranes subjected to air jet impingement*. International Journal of Heat and Mass Transfer, 2013. **58**(1-2): p. 300-311.
 12. Plawsky, J., A. Fedorov, S. Garimella, H. Ma, S. Maroo, L. Chen, and Y. Nam, *Nano-and Microstructures for Thin-Film Evaporation—A Review*. Nanoscale and microscale thermophysical engineering, 2014. **18**(3): p. 251-269.
 13. López-Ortega, A., E. Lottini, C.d.J. Fernandez, and C. Sangregorio, *Exploring the magnetic properties of cobalt-ferrite nanoparticles for the development of a rare-earth-free permanent magnet*. Chemistry of Materials, 2015. **27**(11): p. 4048-4056.
 14. Sagawa, M., S. Hirose, H. Yamamoto, S. Fujimura, and Y. Matsuura, *Nd-Fe-B permanent magnet materials*. Japanese journal of applied physics, 1987. **26**(6R): p. 785.
 15. Kato, H., T. Akiya, M. Sagawa, K. Koyama, and T. Miyazaki, *Effect of high magnetic field on the coercivity in sintered Nd-Fe-B magnets*. Journal of Magnetism and Magnetic Materials, 2007. **310**(2, Part 3): p. 2596-2598.
 16. Kneller, E.F. and R. Hawig, *The exchange-spring magnet: a new material principle for permanent magnets*. IEEE Transactions on Magnetics, 1991. **27**(4): p. 3588-3560.
 17. U.S.-Energy-Information-Administration. *Annual Energy Outlook*. 2016; Available from: <https://www.eia.gov/totalenergy/>.

18. Ruzmetov, D., K.T. Zawilski, V. Narayanamurti, and S. Ramanathan, *Structure-functional property relationships in rf-sputtered vanadium dioxide thin films*. Journal of Applied Physics, 2007. **102**(11): p. 113715.
19. Okimura, K., T. Watanabe, and J. Sakai, *Stress-induced VO₂ films with M2 monoclinic phase stable at room temperature grown by inductively coupled plasma-assisted reactive sputtering*. Journal of Applied Physics, 2012. **111**(7): p. 073514.

Chapter 2. High Heat Flux Evaporation through Nanoporous Membranes

2.1 Introduction

Evaporation is a ubiquitous phase changing mode of heat transfer that is capable of dissipating high heat fluxes. Boiling heat transfer [1, 2], while also a phase changing mode of heat transfer, has instability issues such as severe temperature and pressure fluctuations that are dissociated in evaporation, which make it a more desirable heat transfer mode for high heat flux thermal management devices. Flat plate vapor chambers, also referred to as thermal ground planes (TGP), use vapor to spread concentrated heat from hot spots and have been intensively explored [3]. Increasing evaporative heat flux is especially important given that there are an even increasing power and heat flux on contemporary and emerging electronic devices for commercial and defense applications, such as light-emitting diodes (LEDs) [4], laser diodes [5], power amplifiers [6], high electron mobility devices (HEMD) [7], etc. In many of these devices, both cases of overall heat flux exceed 100 W/cm^2 and localized heat fluxes greater than 500 W/cm^2 (hot spots) are developing into immediate challenges to face [8]. A rational strategy to enhance the efficiency of the evaporator, a key component of TGP, is increasing the effective evaporating area.

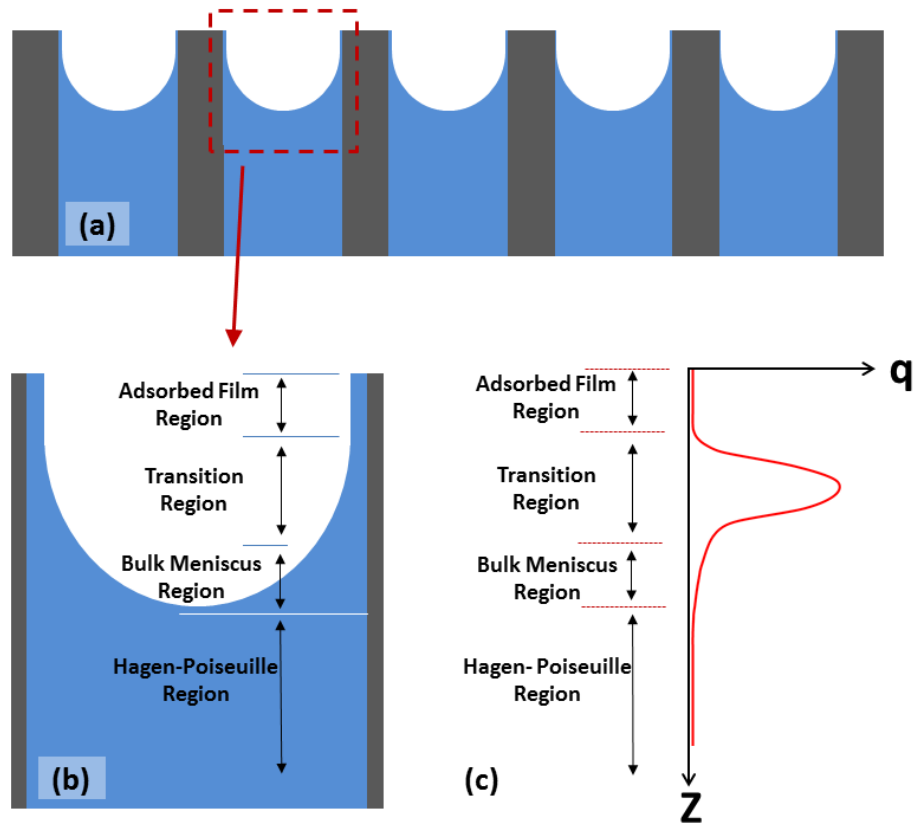


Figure 2.1 Heat flux inside of nano pores as a function of depth: (a) a schematic of menisci inside nano pores (b) an enlarged schematic of menisci in a nano-channel (c) The heat flux as a function of depth that is also conjoined with the liquid film thickness.

High heat flux evaporation only occurs within a small region around the triple-phase point (solid, liquid, vapor contact points). As shown in Figure 2.1 (b) and (c), only a small ‘thin film’ region along a vapor-liquid meniscus has efficient evaporative heat dissipation while the thicker liquid layer in the intrinsic meniscus region acts as a large thermal resistance [9] and a very thin region referred to as “adsorbed thin film region”, comprising of only one to a few monolayers of water molecules, has strong

attractive solid-liquid interactions which prevent the liberation of water molecules. This schematic has been analyzed and verified through molecular dynamic simulations on a variety of fluids such as FC-72 [10], water [11, 12], liquid argon [13] and R141b [14]. Because the portion of the evaporating thin film region is relatively small in a bulk liquid pool, micro and nano-structures have been suggested as an effective means to confine the size of the liquid-vapor menisci and enhance the relative portion of the evaporating thin film regions [9].

A variety of micro and nanostructured wicks have been explored, especially for evaporator applications in vapor chambers, such as sintered copper particles [15, 16], porous copper particles [17], micron sized-Si pillars [8, 18], and carbon nanotubes [19]. Several recent studies achieved heat fluxes close to $1\text{kW}/\text{cm}^2$. However, in most cases either the wall superheat was large ($50\text{K}\sim 160\text{K}$) or the heat input area was small ($0.006\sim 0.1\text{cm}^2$) [8, 15-17, 20, 21]. The largest heating area that was able to achieve a heat flux close to $1\text{kW}/\text{cm}^2$ was 0.32cm^2 with a heat flux of $990\text{W}/\text{cm}^2$ using a sintered copper wick and a superheat of 147K [15]. The smallest wall superheat while achieving close to $1\text{kW}/\text{cm}^2$, was less than 5K but on a heating area of 0.006cm^2 . In most of these studies, the wicking structures were fabricated on a two-dimensional plane and the cooling liquid was supplied along the surface. In such configurations, the working fluid can sufficiently reach the center of the hot spot if the heating area is small. However, when the heat input area is too large, and the working fluid has to travel a long distance along the surface, the liquid can dry out and therefore unable to reach the center of the heated area would emerge [8].

Nanoporous membranes have been suggested as a promising candidate for attaining a high evaporative heat flux [22-24]. Evaporation through a nanoporous membrane provides benefit of decoupling the capillary driven force and viscous pressure drop for liquid flow, as the former is dictated by the pore size and the latter is controlled by the pore size as well as the membrane thickness. Contemporary lithographic technologies and self-assembling processes enable rational designs for optimal pore size, porosity, and thickness. In a vapor chamber, the membranes can be integrated with microchannels, such that liquid can be supplied laterally to the hotspots through the microchannels with a small pressure drop while being driven by the large capillary force in the nanopores. Theoretical studies by Lu et al. [24] and Hanks et al. [23] showed very high critical heat flux (CHF) can be achieved. Despite this great promise, little experimental data is available. Of the available experimental data, a heat flux of $96\text{W}/\text{cm}^2$ for IPA evaporation (based on the pore area) [25] was the highest achieved so far and is still far below the theoretical CHF value [26]. Therefore, the further experimental investigation is needed to test the feasibility of high flux evaporation through nanopores.

In this work, we carried out experimental evaporative heat transfer using IPA as the working fluid and AAO membranes that had an area of 0.5cm^2 and an average pore size of 200nm. We demonstrated a high evaporative heat flux of $210\text{W}/\text{cm}^2$ based on the overall AAO surface area or nearly $400\text{W}/\text{cm}^2$ based on the pore area. Importantly, this heat flux is close to the theoretical value of $570\text{W}/\text{cm}^2$ (based on the pore area) for IPA evaporation through nanoporous membranes. Time synchronized high-speed

images verified that evaporation was the main heat transfer mode in the high heat flux regime.

2.2 Experimental

2.2.1 Characterization of AAO membrane

AAO membranes with nominal average pore size of $0.2\mu\text{m}$ were purchased from Sigma Aldrich (Whatman, 6809-6022). The membrane was characterized by FEI XL30 SEM (scanning electric microscope). The Figure 2.2 (a) show the top view of the membrane after the platinum heater layer deposition in different magnification. Figure S1 (b) shows the pore boundaries determined by image J software. The calculated porosity after Pt heater deposition was 0.52. Figure S1 (c) and (d) show the cross

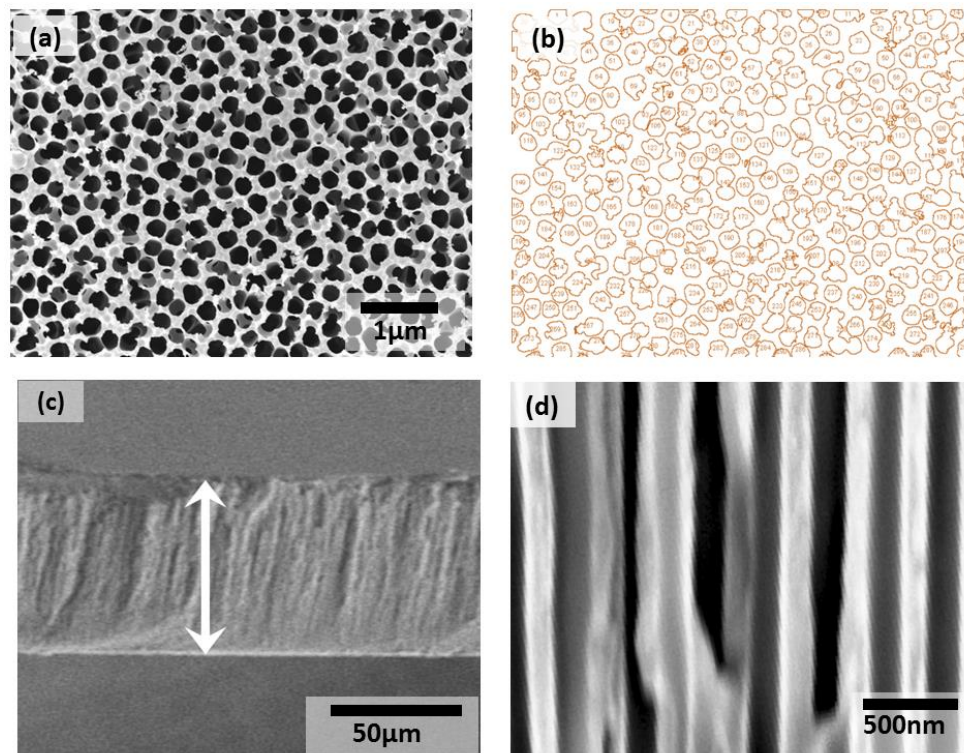


Figure 2.2 SEM images of AAO membrane (a)After Pt heating layer deposition. (b) Pore boundaries determined by Image J program. (c) An overview of cross section image of the AAO membrane. (d) A closed view of AAO membrane cross section.

sections of the membrane. Figure S1 (c) shows that the thickness of the membrane was about 50 μm , and (d) shows that the diameters of the channels were between about $200\text{nm}\pm 30\text{nm}$.

2.2.2 Preparing wick sample

The membrane was attached to a PMMA block that has $71\text{mm} \times 71\text{mm}$ square hole as shown Figure 2.3 (a). In this step, Torr Seal® Low Pressure epoxy was applied with blade casting method on the acrylic block as shown Figure 2.3 (b), and then an AAO membrane was attached to the top of the acrylic block as shown Figure 2.3 (c). Pores of the membrane overlapped with the PMMA block were closed with the epoxy

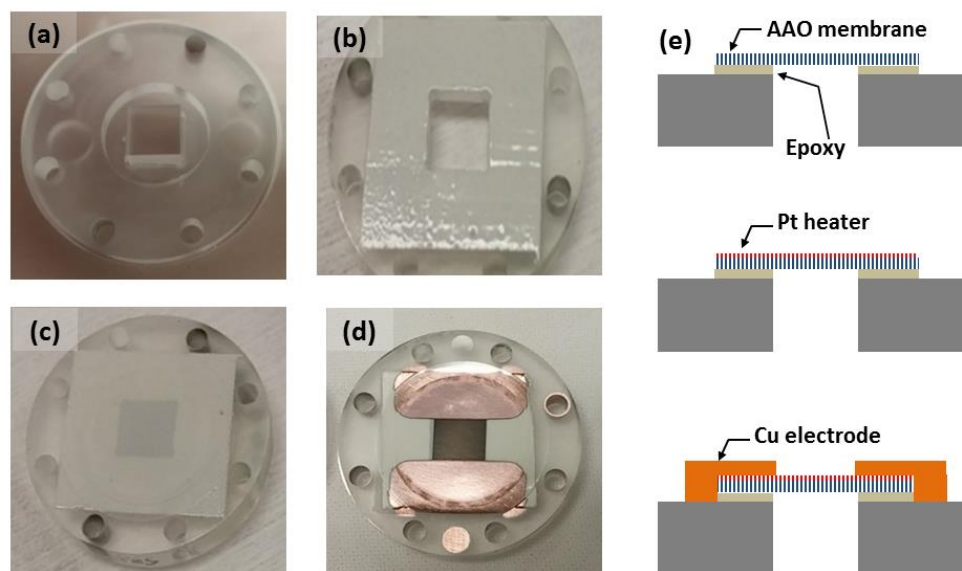


Figure 2.3 Wick sample preparation detail. (a) An image of the sample holder. (b) After Torr Seal® epoxy was applied on the top of the sample holder by blade casting (c) After AAO membrane was attached to the sample holder. (d) After Pt heater and Cu electrode was sputter deposited using shadow masks. (e) Overall schematics of wick sample preparation.

and became inactive for evaporation. Only pores at the center became active. Using a shadow mask, which has a 0.5cm^2 open area, about 2~3 nm thick chrome layer was deposited via PVD as an adhesive layer. Then 30 nm of platinum layer was deposited on the top of the adhesion layer. Using a second mask, about $2\mu\text{m}$ thick copper contact pads were deposited as shown Figure 2.3 (d). Figure 2.3 (e) shows overall schematics of wick sample preparation. The internal resistivity of each of the contact pads was less than 0.1 ohm/cm, whereas the resistance of the heater layer was about 40~70 ohm depends on samples so that the contact pads do not dissipate heat when a large power is applied.

We used AAO for the nanoporous membranes and IPA as the working fluid for our evaporative heat transfer experiments. IPA was chosen due to its excellent dielectric properties and high wettability. The heat transfer setup is schematically shown in Figure 2.4 (a). The setup is similar to the work done by Xiao *et al.* [25], but has significant modifications.

A thin, 30nm thick Pt layer was deposited on top of the AAO membrane to serve as both a heater and a thermometer. The Pt layer only coated the solid portion of the AAO and did not change the pore size. To ensure efficient heat transfer and eliminate potential premature dry out, we eliminated the inactive edge area on the AAO with the addition of an aligned heating layer deposition using a shadow mask as shown in Figure 2.4 (c). The test assembly was then placed in a vacuum chamber as shown in Figure 2.4 (b). The test apparatus was made of clear acrylic, so the fluid level was visible to ensure liquid delivery from the external reservoir to the AAO membranes to prevent

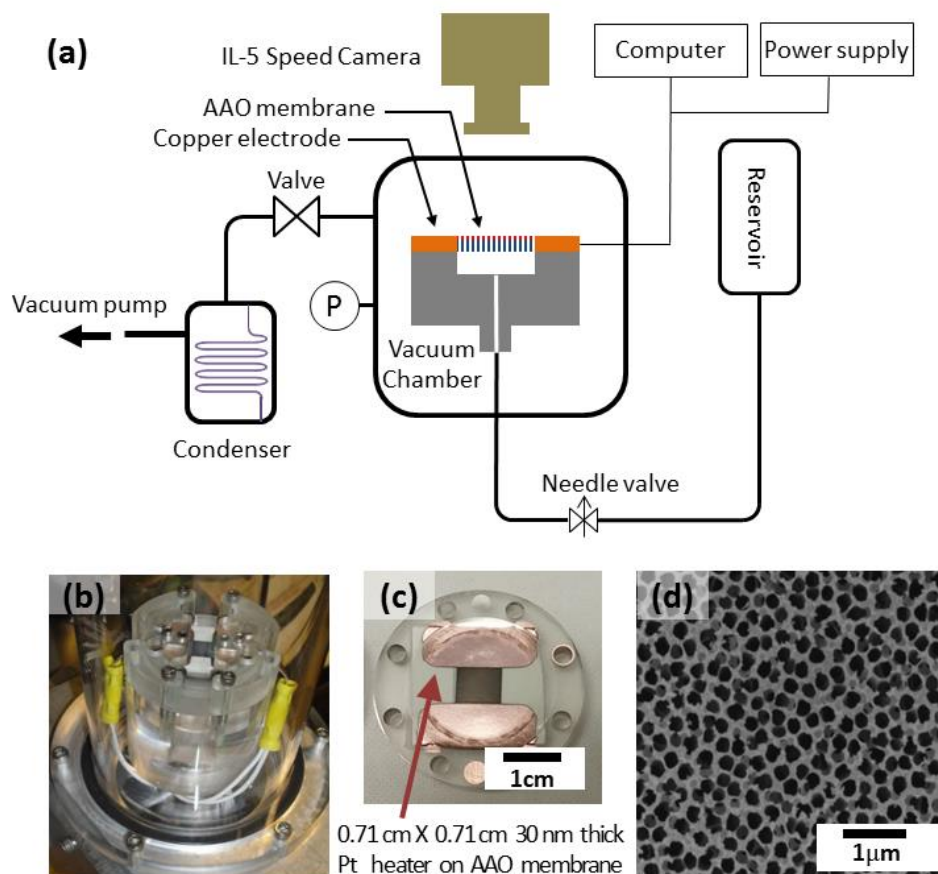


Figure 2.4 Experimental set up: (a) Overview of set up schematic. (b) Image of the testing apparatus placed in the vacuum chamber. (c) Image of a wicking sample. (d) SEM image of the AAO membrane.

premature dry out. A view port was installed on the top of the chamber to take slow motion images with an IL-5 camera (Festec Imaging, 250frames/second). More details on the sample preparation are described in the Supplemental Materials.

The chamber was initially pumped down to approximately 3 Pa before the IPA was supplied from an external reservoir to reach the AAO membrane. Upon the delivery of the liquid, the pressure was stabilized at 40Pa. After the liquid completely wet the membrane, a DC power supply (Agilent 6575A #J09) was used to apply heating power

to the Pt thin film heater on the AAO. The power was increased stepwise with a 5W interval. The temperature of the membrane was measured by monitoring the resistance change of the Pt heater using pre-calibrated temperature-resistance curves (Figure 2.6). When the system reached steady state (usually within ten seconds) after applying the heating power at each step, the temperature was recorded continuously for two minutes after it was stabilized. We also confirmed that the heat loss through the fixture was small ($\sim 0.007\text{W/K}$, see Supplementary Materials).

2.2.3 Experimental setup

Figure 2.5 shows the schematics of the electrical connection on the sample. The wick assembly prepared as shown in Figure 2.5 (d) was mounted on the liquid supply channel using an o-ring and screws as shown Figure 2.5 (b and c). The experiment was designed for testing high-power heat dissipation. Therefore resistances caused by electrical connection potentially produce large heat. By utilizing thick tin plate as deforming contact pad and firmly clamped on the copper electrode on the wick assembly, we ensured that contact resistance was less than 0.1ohm. The measured resistance in the entire connection was about 0.2 ± 0.01 ohm which was less than 0.7% of the resistance of the heating layer. The maximum current that was applied during the experiment was about 1.5 amps; therefore the maximum heat dissipated through the electrical wire was less than 0.5 W when 103 W was applied.

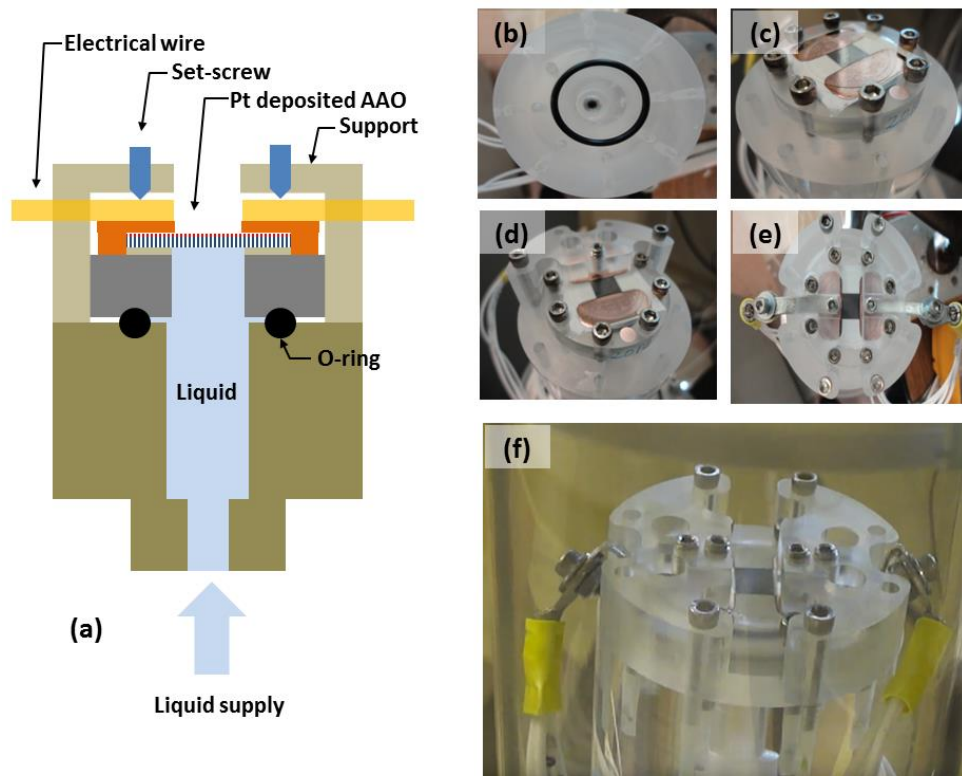


Figure 2.5 Liquid supply channel and electrical wire connection. (a) Schematics of connections. (b) Liquid channel body. (c) After the wick sample is mounted on the liquid channel body (c) After one side of electrical connection-clamp is installed. (d) Electrical wires are clamped (f) overview of the sample assembly.

The temperature coefficient of resistance (TCR) of the Pt layer was calibrated using a programmable convection oven. Electrical connection was made on both sides of the copper electrode, and a K-type thermocouple was placed on the membrane less than 1mm height above. The resistance and temperature change of the platinum were recorded using an Agilent 34401A multimeter and NI USB-TC01 data acquisition module. The temperature was increased 5K each step, and each temperature was held for about two and half hour so that the temperature and the resistance were stabilized. The calibrated TCR value was 0.0011/K.

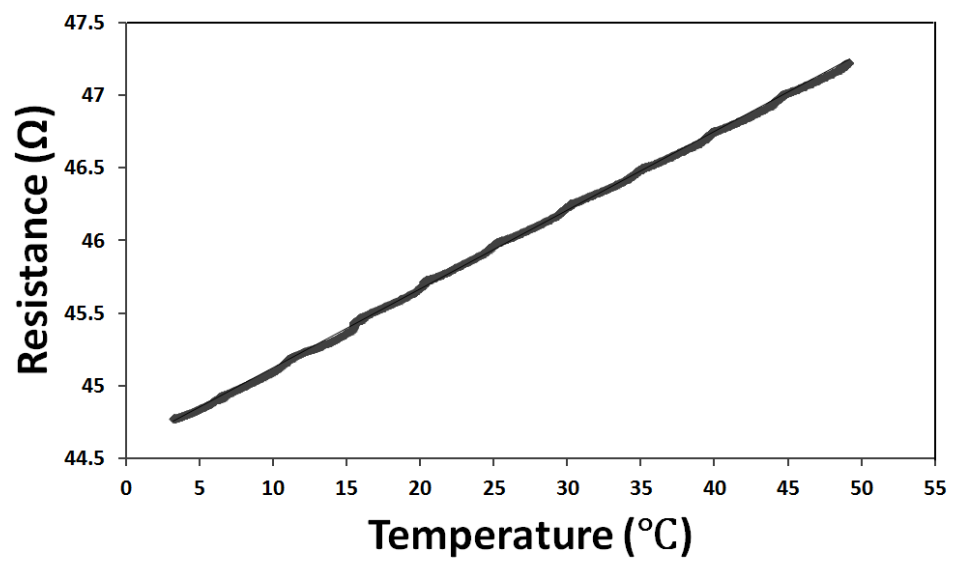


Figure 2.6 Temperature and resistance calibration curve of the Pt heater.

2.3 Results and Discussion

2.3.1 Observed heat transfer regimes depend on applied power

Figure 2.7 depicts the dissipated heat flux as a function of the temperature of the heater. To develop an understanding of the heat transfer mechanism, high-speed images are coordinated with the heat dissipation curve, as shown Figure. 2.9. Dynamic temperature profiles at different heat fluxes were recorded and shown in Figure 2.8. Based on the heat transfer behavior and the visual images, we can divide the heat transfer into three working regimes under different heat flux conditions.

Liquid flooding, driven by the pressure difference across the membrane, was

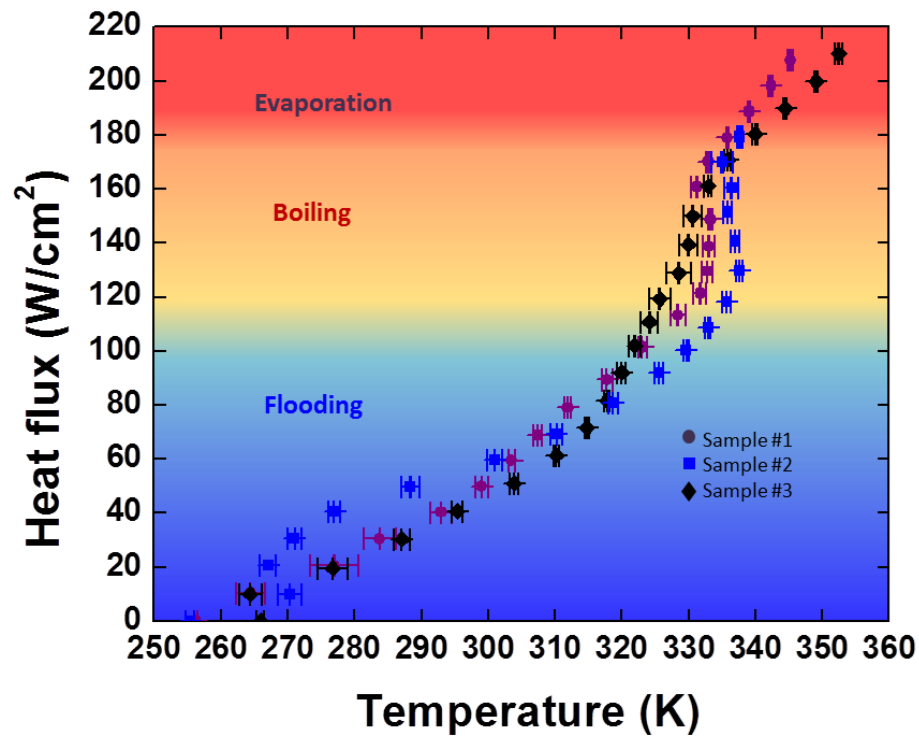


Figure 2.7 Summarized heat dissipation versus temperature.

observed from the beginning of the experiment until heat dissipation reached around $110\text{W}/\text{cm}^2$ as shown Figure 2.9 (a). The pressure difference between the top and the bottom of the membrane was about 100 kPa because the liquid was supplied from an external fluidic reservoir at atmospheric pressure to the bottom of the membrane while the top of the membrane exposed in the 40 Pa vacuum. In this flooding regime, due to the irregular pattern of the flooding, the temperature of the membrane fluctuated immensely ($>5\text{K}$) as shown in Fig. 5, especially for heat fluxes below $30\text{W}/\text{cm}^2$ temperature fluctuation was $\sim 15\text{K}$. At low heat flux, the liquid transport rate due to the pressure difference across the membrane exceeded the evaporation rate. Thus liquid puddle formed the top of the membrane. As heat flux reached $110\text{W}/\text{cm}^2$, the evaporation rate was close to liquid transport rate, and flooding gradually ceased. Heat transfer in this regime was mainly due to the evaporation from the liquid puddle and convection due to the flooding. However, the contribution of convective is not significant.

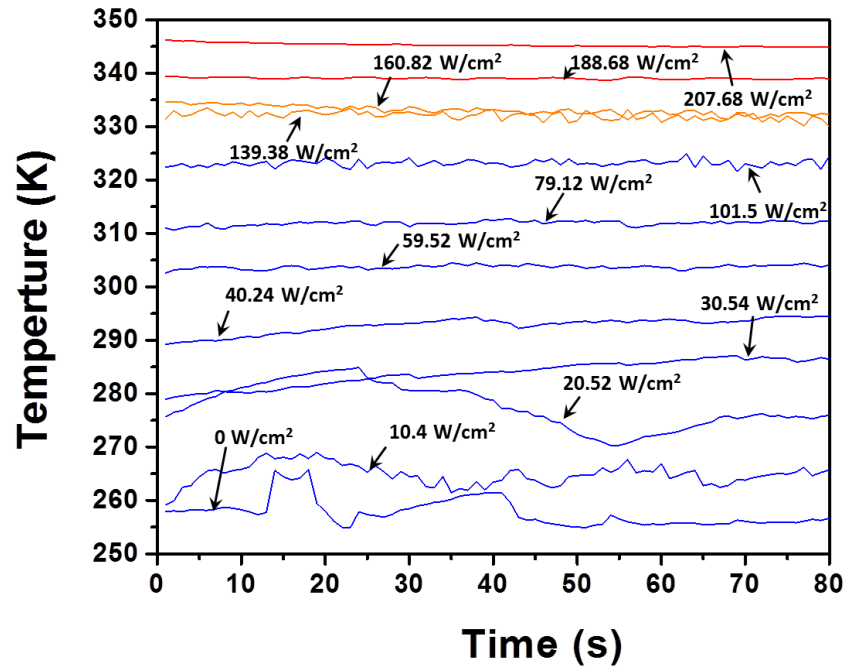


Figure 2.8 Temperature dynamic at various heating power.

After the heat flux was increased to above $\sim 110 \text{ W/cm}^2$, flooding was no longer observed, and the heat transfer entered into the second regime in which microscale boiling and bubble nucleation occurred on top of the membrane as shown in Figure 2.9 (c) and (d). In this regime, increasing the heat flux did not further increase the membrane temperature (Figure 2.7); the membrane temperature remained almost constant which is shown in the dynamic temperature profile (top lines in Figure 2.8). In this micro-scale boiling regime, when the heat flux was in the range of 110 to 160 W/cm^2 , the temperature of the membrane reached $330 \pm 5 \text{ K}$. The saturation temperature of IPA at 40 Pa is $\sim 236 \text{ K}$ accordingly to the Clausius-Clapeyron equation, and the fact that the nucleation was formed at a considerably higher temperature (330 K)

shows that the nucleation was homogeneous. This is not surprising given that IPA is highly wetting on AAO. Previous studies have also demonstrated homogeneous nucleation on highly wetted surfaces [27, 28]. As the mode of heat transfer shifted into boiling, the slope of the heat dissipation curve in Figure 2.7 sharply increased, indicating the enhancement of the heat transfer coefficient. Similar observations are also reported by others [8, 25].

When the heat flux was increased to $\sim 170\text{W}/\text{cm}^2$, dried region started appearing as shown in Figure 2.9 (e). Full receding of menisci into the bottom of the membrane which condition often referred as ‘dry out’ would cause sharp increasing of temperature of the membrane or instant burning out of the membrane. However, the nearly constant temperature profile as shown Figure 2.8 (red line) suggests that the temperature of the membrane was maintained by steady evaporation. We hypothesize that, the evaporation rate balanced with liquid transport rate, and the liquid menisci were pinned at the top of the pores as illustrated in Figure 2.1 (a) thus the top surface appeared to be dried, but steadily evaporation occur from the thin film region of the meniscus interface as illustrated in Figure 2.2 (a). Our best performing sample displayed a temperature fluctuation below 0.5K for an extended period. Further increasing of heat flux beyond the $170\text{W}/\text{cm}^2$ still did not cause ‘dry out,’ but the region that was appeared to be dried was expanded to a larger area as shown in Figure 2.9(f) while the temperature profile shifted into higher temperature range as shown Figure 2.8 (red line). Even the evaporation rate exceeds the liquid transport rate due to the pressure difference across the membrane, the capillary pressure ($\sim 400\text{kPa}$) would maintain the menisci pinned at

the top of the membrane or slightly extended from the top unless heat flux exceeds CHF and liquid supply cannot be sustained. In our experiments, the obtained CHF values ranged from 190 to 210W/cm² for three AAO membrane samples that have average pore size of 200nm and a ~52% porosity (Section 1 in the Supplementary Materials). The temperature of the membrane at dry-out was 355K. The onset of CHF was evidenced by instant burnt out of the sample when the applied power was further increased beyond the CHF.

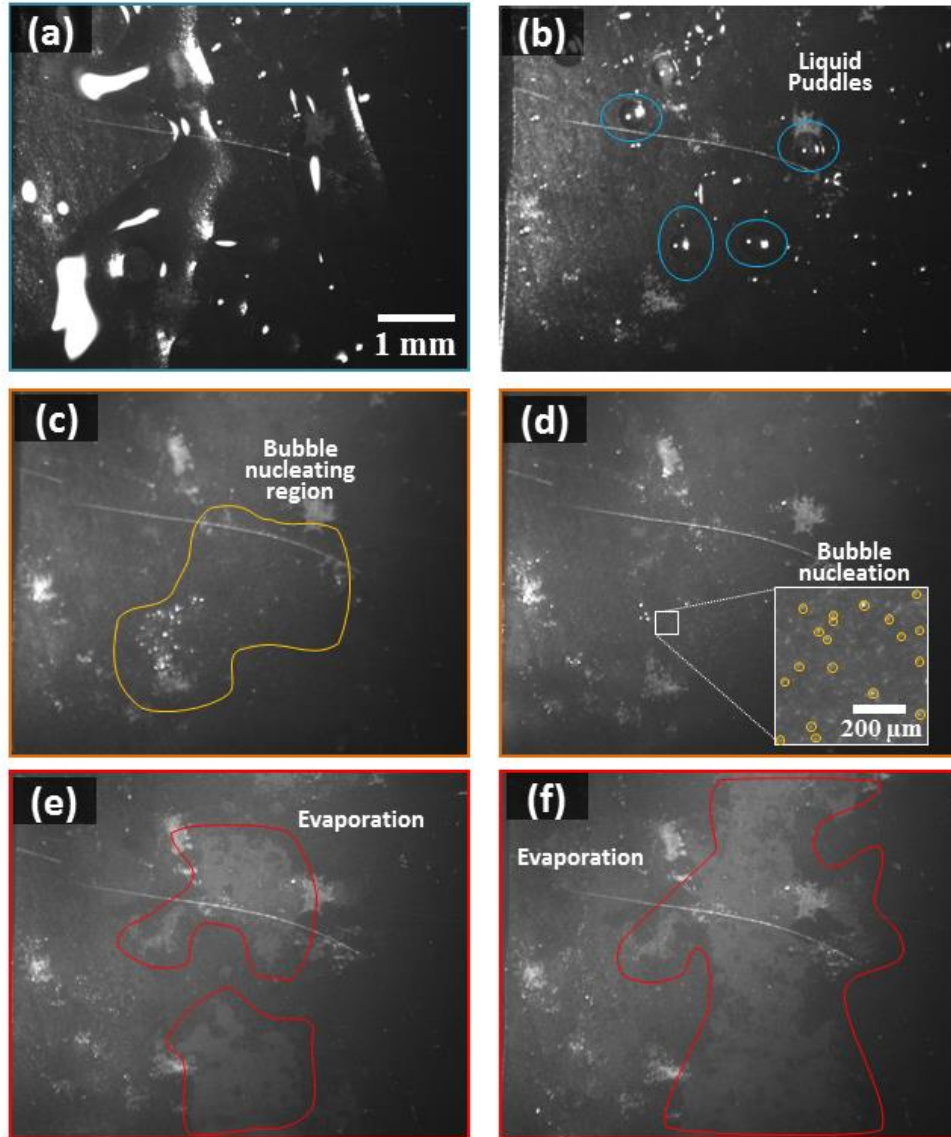


Figure 2.9 Images of the membrane surface at various heat dissipating regimes: The images are taken at 250 frames per second (FPS) by FastecImaging IL-5 high-speed camera. The main mode of heat transfer at each of the images is (a) Flooding, $q = 9.7 \text{ W/cm}^2$. (b) Flooding, $q = 40.6 \text{ W/cm}^2$. (c) Micro scale boiling, $q = 129.9 \text{ W/cm}^2$. (d) Micro scale boiling, $q = 151.5 \text{ W/cm}^2$. (e) Evaporation, $q = 170.1 \text{ W/cm}^2$. (f) Evaporation, $q = 179.4 \text{ W/cm}^2$.

The obtained CHF value ($\sim 210 \text{ W/cm}^2$) is significantly higher than what was previously obtained in similar experiments that used IPA on AAO membranes. If we take the porosity of the AAO membranes ($\sim 52\%$) into account, the CHF value based on the pore area is $\sim 420 \text{ W/cm}^2$, about a 4-fold increase compared to which was what was achieved in a previous work (a heat flux of 96 W/cm^2), [25].

2.3.2 Comparison between the experimental result and the theoretical value

To put this value into perspective, it is necessary to compare this to the theoretical value. For the nanoporous membrane configuration in this work, liquid movement inside the pores is driven by the passive capillary force as well as the $\sim 100 \text{ kPa}$ pressure difference across the membrane, and it also encounters a flow resistance along the pore channel during liquid movement. The CHF is reached when the liquid feeding force and the viscous drag are balanced. At this critical state, the liquid-vapor interface is fully extended, and the curvature of the interface profile has similar value to the inverse of pore radius because IPA has a near-zero contact angle with a metal oxide. Therefore, the liquid transport driven pressure can be calculated by

$\Delta P_{dri} = \frac{4\gamma}{d} + 1 \text{ atm} = 529 \text{ kPa}$ where $d = 200 \text{ nm}$ is the pore diameter, $\gamma = 21.4 \times 10^{-3} \text{ N/m}$ is the liquid surface tension, and 1 atm accounts for the pressure difference between the liquid reservoir and the vacuum chamber. By assuming a constant density

for the liquid, the viscous pressure drop along the pore channel can be calculated by the

Hagen-Poiseuille equation as $\Delta P_{vis} = \frac{32\mu L v}{d^2} = \frac{32\mu L}{d^2} \frac{q''}{h_{fg}\rho_l}$, where $\mu = 1.33 \times 10^{-3} \text{ Pa}\cdot\text{s}$

is the liquid viscosity, $\rho_l = 786 \text{ kg/m}^3$ is the liquid density, $h_{fg} = 732 \text{ kJ/kg}$ is the

latent heat of evaporation, $L = 50 \mu m$ is the pore length (or membrane thickness). When $\Delta P_{vis} = \Delta P_{dri} = 529 kPa$, the heat flux over the pore area is $q''_{CHF} = 572 W/cm^2$.

Besides liquid transport limit, there is also a kinetic limit for evaporation as calculated by [27] $q'' = \frac{2\sigma}{2-\sigma} h_{fg} \sqrt{\frac{M}{2\pi R} \left(\frac{P_{l,corr}}{\sqrt{T_l}} - \frac{P_v}{\sqrt{T_v}} \right)}$, where σ is the accommodation coefficient of liquid, h_{fg} is the latent heat of evaporation, M is the molar mass, R is gas constant. P_v and T_v are the pressure and temperature of far field vapor and $P_{l,corr}$ and T_l are the corrected pressure and temperature of liquid near the liquid-vapor interface, $P_{l,corr} = P_l \times \exp\left(-\frac{2\gamma M}{rR\rho_l T_l}\right)$ according to Kelvin's equation for pressure change at a curved liquid-vapor interface where P_l is the bulk liquid pressure and is assumed to be 1 atm based on our experimental configuration. With a characteristic coefficient value of $\sigma = 0.1$, the kinetic limit result is $q'' \approx 1400 W/cm^2$ and is 2 times larger than the fluid transport limit, which means the CHF of our current experiment is mainly limited by the fluid transport.

Comparing the experimental results of this work ($\sim 400 W/cm^2$) with the theoretical maximum heat flux ($572 W/cm^2$), there still remains a discrepancy between these values. Some probable causes are the complex shape of liquid-vapor interface, the large temperature difference across the AAO membrane thickness due to the low thermal conductivity of alumina irregularity of pore shape (as shown in Figure 2.2(d)), local hotspots caused by blocked pores or misalignment of the heated area and the porous membrane, bending and crack of membrane due to thermal expansion at high

operating temperature, mechanical failure of the membrane caused by large pressure difference, etc. Nevertheless, the experimental CHF in this work has the same order of magnitude with the theoretical value, and our experimental work is approaching the theoretical CHF in liquid-vapor phase change heat transfer experiments. We proved that a nanoporous membrane evaporation device with a cross-plane liquid supply is an efficient way to achieve a steady and uniform high heat flux removal. With the proper mechanical support, as well as circulation components such as a condenser and a liquid feed wick structure, nanoporous membranes could be used in thermal ground plane systems or heat pipes and be able to dissipate high heat fluxes from devices with a much lower temperature and larger area. Higher heat fluxes could be achieved by reducing pore size and increasing porosity to provide a larger evaporation area, decreasing the membrane thickness to reduce the flow resistance inside the pores, replacing IPA with other fluids that have a larger accommodation coefficient and latent heat. The gap between the experimental and theoretical CHF might also be narrowed by replacing the AAO membrane with a material that has a higher thermal conductivity (as discussed in SI section 6) and better mechanical properties, optimizing the pore size and porosity to balance the needs for less viscous loss and larger capillary force, and by thorough and accurate modeling and calculation of the CHF in this experimental configuration.

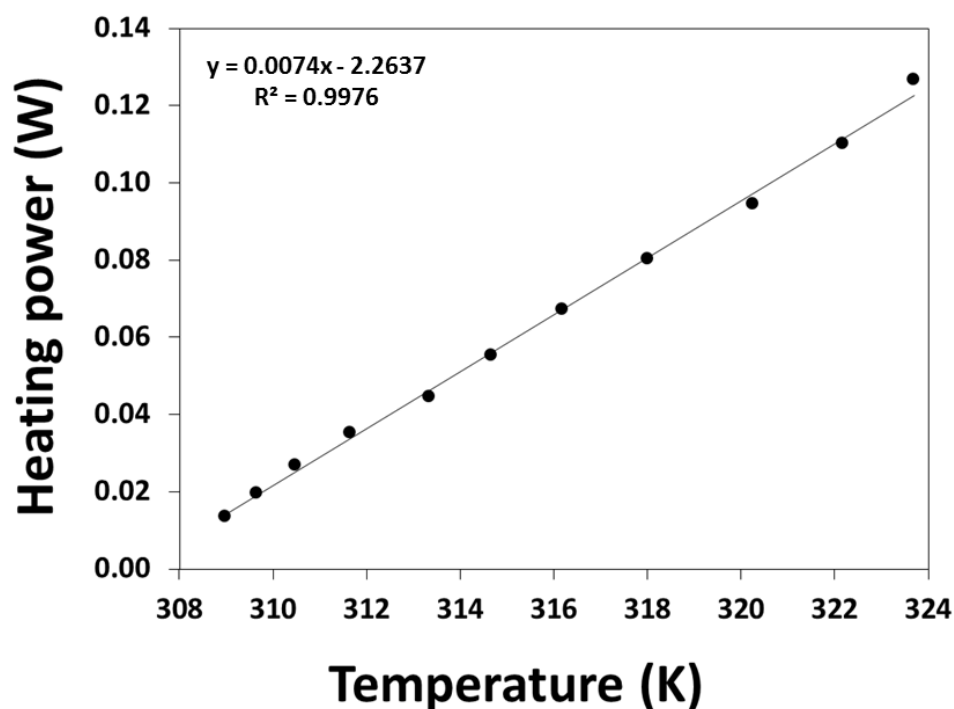


Figure 2.10 Heat loss through the fixture without liquid supply.

Aside from phase-change of liquid, the applied heat flux during the experiment could be dissipated by conduction through the experimental fixture, convection of the liquid, and splashing of the liquid droplet, all of which could cause heat loss and thusly overestimation of the phase-change heat flux. We conduct heat loss analysis for all of them as described below.

The heat loss through the fixture was measured by heating one sample in the experimental chamber with the same conditions except without liquid supply. In order to avoid membrane overheat, the applied heating power was small. It showed the a good linear relation between heating power and membrane temperature as shown in Fig. S5 and the heat loss through fixture by conduction was $\approx 0.007\text{W/K}$. The maximum

temperature change during the whole experiment was below 110K, indicating maximum heat loss of less than 0.77W which is negligible compared with the heating power we applied.

Liquid travels upwards inside a square-shaped channel with a cross-section area of 0.5cm^2 and then touches the bottom of the membrane. Under maximum heat flux condition ($q'' = 210\text{ W/cm}^2$), liquid transport velocity inside this channel can be calculated by $u = \frac{q''}{\rho l h_{fg}} = 3.6 \times 10^{-3}\text{ m/s}$. Reynolds number of this flow is $\text{Re} = \frac{\rho l u d_h}{\mu} = 14.9$ where d_h is the hydrolic diameter of fluid channel and the is equal to the side length (0.7cm) for a square. Due to the small Reynolds number, we can assume the convection loss through liquid is nearly natural convection. Kadambi and Drake gave the natural convection equation for a heated horizontal plate facing down[ref: Mills & Coimbra book] as $\text{Nu} = 0.82\text{Ra}^{1/5}$ where $\text{Nu} = \frac{hl}{\lambda}$ and $\text{Ra} = \text{Gr} \cdot \text{Pr} = \frac{gl^3\beta\Delta T}{\nu^2} \cdot \frac{\nu}{\alpha} = \frac{gl^3\beta\Delta T}{\nu\alpha}$ in which h is the heat transfer coefficient, g is the gravatational acceleration, l is the characteristic length and is equal to the side length of the square, ΔT is the temperature difference between the heated surface and bulk liquid, λ , β , ν , and α are the thermal conductivity, the volume expansion coefficient, the kinematic viscosity, and the thermal diffusivity of the liquid, respectively. Apply IPA physical properties into the equation and use $\Delta T = 110\text{ K}$ which is an overestimation, we have calculated $hA = 0.016\text{ W/K}$, proving the irrelevance of convective loss.

During the experiment, liquid travels from 1atm condition to vacuum chamber, so it will evaporate with low power or even without power supply, and liquid droplet

will splash around and cause heat loss. The observed liquid splashing stopped at 15W (also indicated in Fig. 6 dynamic temperature profile of 30W/cm²). The mass flux driven by pressure difference was $\dot{m} = \frac{15W}{732kJ/kg} = 2.0 \times 10^{-5} kg/s$. Part of this flux splashed and changed to vapor phase somewhere in the chamber, and the rest of it cooled from bulk liquid temperature (room temperature, 298K) to chamber vapor saturation temperature (235.8K). Thus, $732 kJ/kg \times \dot{m}_{splash} = (298 K - 235.8 K) \times c_p \times (\dot{m} - \dot{m}_{splash})$, where c_p is the specific heat of IPA and is equal to $2.6 kJ/kg \cdot K$ and $\dot{m}_{splash} = 7.3 \times 10^{-6} kg/s$. Therefore, the heat loss through liquid splashing was $\dot{q}_{splash} = \dot{m}_{splash} \times h_{fg} = 5.3W$, which is only about 5% of the maximum power supply.

AAO membrane has a thermal conductivity of 1.5W/m·K. When near CHF was applied on the membrane, the temperature difference across the membrane can be determined by $\Delta T = \frac{q''}{1-\phi} \frac{d}{\kappa}$ where ϕ , d and κ are the porosity, thickness, and the cross-plane thermal conductivity of the membrane, respectively. Using the parameters from the characterization of the membrane, the temperature difference between the top and the bottom of the membrane could be as large as 80K. The large temperature difference across the membrane and the low thermal conductivity of the material could dramatically decrease the heat dissipation ability because temperature difference can cause mismatch of thermal expansion and thus mechanical failure, or local hotspot that will burn out the membrane. Utilize highly thermal conductive materials for membrane potentially improve the heat dissipation ability and thus achieve higher heat flux.

2.4 Conclusion

We report an enhanced CHF in a nanoporous membrane configuration. The achieved high critical heat flux on the overall AAO surface area was $\approx 210 \text{ W/cm}^2$ which translates to a critical heat flux of $\approx 400 \text{ W/cm}^2$ if only the pore area is considered, which is much closer to the theoretical maximum heat flux of 521.9 W/cm^2 . This improvement compared with the previous study [25] could be attributed to the sample preparation process which carefully eliminated possible inactive areas. Our demonstration suggests that the nanoporous membrane evaporation device with a cross-plane liquid supply is an efficient way to dissipate heat fluxes on a relatively large area ($\approx 0.5 \text{ cm}^2$). Higher heat fluxes could be achieved by reducing pore size and increasing the porosity to provide a larger evaporation area, and also by decreasing the membrane thickness. Contemporary lithographic technologies and self-assembling processes enable rational designs for optimal pore size, porosity, and thickness. Therefore, nanoporous membrane configuration could be effectively utilized in high heat flux thermal management devices.

2.5 Acknowledgements

We wish to acknowledge useful discussion with Dr. Edward Dechaumphai who helped us a lot at the beginning of this project.

This chapter, in full, is currently being prepared for submission for publication of the material. Young Jin Kim, Qingyang Wang, Kristine McGrath, Renkun Chen. The dissertation author was the primary investigator and author of the paper.

2.6 References

1. Chen, R., M.C. Lu, V. Srinivasan, Z. Wang, H.H. Cho, and A. Majumdar, *Nanowires for Enhanced Boiling Heat Transfer*. Nano Letters, 2009. **9**(2): p. 548-553.
2. Wu, H.Y. and P. Cheng, *Boiling instability in parallel silicon microchannels at different heat flux*. International Journal of Heat and Mass Transfer, 2004. **47**(17-18): p. 3631-3641.
3. de Bock, H.P.J., S. Chauhan, P. Chamarthy, S.E. Weaver, T. Deng, F.M. Gerner, M.T. Ababneh, and K. Varanasi. *On the Charging and Thermal Characterization of a micro/nano structured Thermal Ground Plane*. in *Thermal and Thermomechanical Phenomena in Electronic Systems (ITherm), 2010 12th IEEE Intersociety Conference on*. 2010. IEEE.
4. Arik, M., J. Petroski, and S. Weaver. *Thermal challenges in the future generation solid state lighting applications: light emitting diodes*. in *Thermal and Thermomechanical Phenomena in Electronic Systems, 2002. ITherm 2002. The Eighth Intersociety Conference on*. 2002.
5. Shen, L., H. Chen, F. Xiao, Y. Yang, and S. Wang, *The step-change cooling performance of miniature thermoelectric module for pulse laser*. Energy Conversion and Management, 2014. **80**: p. 39-45.
6. Cotler, A.C., E.R. Brown, V. Dhir, and M.C. Shaw, *Chip-level spray cooling of an LD-MOSFET RF power Amplifier*. IEEE Transactions on Components and Packaging Technologies, 2004. **27**(2): p. 411-416.
7. Wang, X.D., W.D. Hu, X.S. Chen, and W. Lu, *The Study of Self-Heating and Hot-Electron Effects for AlGaIn/GaN Double-Channel HEMTs*. IEEE Transactions on Electron Devices, 2012. **59**(5): p. 1393-1401.
8. C'oso, D., V. Srinivasan, M.-C. Lu, J.-Y. Chang, and A. Majumdar, *Enhanced Heat Transfer in Biporous Wicks in the Thin Liquid Film Evaporation and Boiling Regimes*. Journal of Heat Transfer, 2012. **134**(10): p. 101501-101501.
9. Plawsky, J., A. Fedorov, S. Garimella, H. Ma, S. Maroo, L. Chen, and Y. Nam,

Nano-and Microstructures for Thin-Film Evaporation—A Review. Nanoscale and microscale thermophysical engineering, 2014. **18**(3): p. 251-269.

10. Maroo, S.C. and J.N. Chung, *Heat transfer characteristics and pressure variation in a nanoscale evaporating meniscus*. International Journal of Heat and Mass Transfer, 2010. **53**(15-16): p. 3335-3345.
11. Narayanan, S., A.G. Fedorov, and Y.K. Joshi, *Interfacial Transport of Evaporating Water Confined in Nanopores*. Langmuir, 2011. **27**(17): p. 10666-10676.
12. Fu, T., Y. Mao, Y. Tang, Y. Zhang, and W. Yuan, *Molecular dynamics simulation on rapid boiling of thin water films on cone-shaped nanostructure surfaces*. Nanoscale and Microscale Thermophysical Engineering, 2015. **19**(1): p. 17-30.
13. Li, L., P. Ji, and Y. Zhang, *Molecular dynamics simulation of condensation on nanostructured surface in a confined space*. Applied Physics A, 2016. **122**(5): p. 1-15.
14. Dong, T., Z. Yang, and H. Wu, *Molecular simulations of R141b boiling flow in micro/nano channel: Interfacial phenomena*. Energy Conversion and Management, 2006. **47**(15-16): p. 2178-2191.
15. Semenic, T. and I. Catton, *Experimental study of biporous wicks for high heat flux applications*. International Journal of Heat and Mass Transfer, 2009. **52**(21-22): p. 5113-5121.
16. Ju, Y.S., M. Kaviany, Y. Nam, S. Sharratt, G.S. Hwang, I. Catton, E. Fleming, and P. Dussinger, *Planar vapor chamber with hybrid evaporator wicks for the thermal management of high-heat-flux and high-power optoelectronic devices*. International Journal of Heat and Mass Transfer, 2013. **60**: p. 163-169.
17. Palko, J.W., C. Zhang, J.D. Wilbur, T.J. Dusseault, M. Asheghi, K.E. Goodson, and J.G. Santiago, *Approaching the limits of two-phase boiling heat transfer: High heat flux and low superheat*. Applied Physics Letters, 2015. **107**(25): p. 253903.

18. Wei, M., S. Somasundaram, B. He, Q. Liang, C.S. Tan, and E.N. Wang. *Experimental characterization of Si micropillar based evaporator for advanced vapor chambers*. in *Electronics Packaging Technology Conference (EPTC), 2014 IEEE 16th*. 2014. IEEE.
19. Cai, Q., C.-l. Chen, G. Xiong, and Z. Ren. *Explorations of carbon nanotube wick structure for high heat flux cooling*. in *ASME 2008 Heat Transfer Summer Conference collocated with the Fluids Engineering, Energy Sustainability, and 3rd Energy Nanotechnology Conferences*. 2008. American Society of Mechanical Engineers.
20. Weibel, J.A., S.V. Garimella, and M.T. North, *Characterization of evaporation and boiling from sintered powder wicks fed by capillary action*. *International Journal of Heat and Mass Transfer*, 2010. **53**(19–20): p. 4204-4215.
21. Hwang, G.S., E. Fleming, B. Carne, S. Sharratt, Y. Nam, P. Dussinger, Y.S. Ju, and M. Kaviany, *Multi-artery heat-pipe spreader: Lateral liquid supply*. *International Journal of Heat and Mass Transfer*, 2011. **54**(11–12): p. 2334-2340.
22. Narayanan, S., A.G. Fedorov, and Y.K. Joshi, *Heat and mass transfer during evaporation of thin liquid films confined by nanoporous membranes subjected to air jet impingement*. *International Journal of Heat and Mass Transfer*, 2013. **58**(1–2): p. 300-311.
23. Hanks, D.F., L. Zhengmao, S. Narayanan, K.R. Bagnall, R. Raj, R. Xiao, R. Enright, and E.N. Wang. *Nanoporous evaporative device for advanced electronics thermal management*. in *Thermal and Thermomechanical Phenomena in Electronic Systems (ITherm), 2014 IEEE Intersociety Conference on*. 2014.
24. Lu, Z., S. Narayanan, and E.N. Wang, *Modeling of Evaporation from Nanopores with Nonequilibrium and Nonlocal Effects*. *Langmuir*, 2015. **31**(36): p. 9817-9824.
25. Xiao, R., S.C. Maroo, and E.N. Wang, *Negative pressures in nanoporous membranes for thin film evaporation*. *Applied Physics Letters*, 2013. **102**(12): p. 123103.

26. Carey, V.P., *Liquid-vapor phase-change phenomena*. 1992: Hemisphere, New York, NY (United States). Medium: X; Size: 645 p.
27. Lin, L., A.P. Pisano, and V.P. Carey, *Thermal Bubble Formation on Polysilicon Micro Resistors*. *Journal of Heat Transfer*, 1998. **120**(3): p. 735-742.
28. Hsu, Y.Y., *On the Size Range of Active Nucleation Cavities on a Heating Surface*. *Journal of Heat Transfer*, 1962. **84**(3): p. 207-213.

Chapter 3. Magnetic core-shell structured MnBi/FeCo exchange spring magnet produced by noble sonic agitation assisted PVD process

3.1 Introduction

Development of sustainable and efficient permanent magnets is crucial for modern technology. Permanent magnets are extensively being used ranging from data recording to transportation. Especially, to replace fossil fuel based engine with an electrical motor for the conserving environment and natural resources, the demand of powerful magnet will increase sharply [1, 2]. Other energy-related applications such as wind power generator and solar panels that track the direction of the sun also highly rely on the supply of permanent magnets [3]. The efficiency of magnets is also directly related to energy consumption. More than half of electrical consumption in the industrial sector is due to electrical motor drives. Considering the fact that industrial sector consumes nearly 30 % of electricity in U.S., Improving strength of permanent magnets which enhance the efficiency of motors by 1% would result in a reduction of nearly 2.2million metric tons of CO₂ emissions and economic saving [2].

The strength of permanent magnets had been improved rather slowly until the 1970s. The maximum energy product, which often referred as $(BH)_{\max}$, and an important parameter that determined the strength of the permanent magnet, increased from ~1MGOe in the 1920s to ~5.5MGOe in 1960s. The most groundbreaking improvement of permanent magnet was achieved in the 1970s and 1980s by utilizing rare earth (RE) element such as Sm and Nd [2, 4]. The $(BH)_{\max}$ of Nd₂Fe₁₄B magnet reached 56MGOe at the end of the 1980s. These RE element increase magneto-crystalline anisotropy when they alloy with transition metals [5].

One of the strongest permanent magnet $\text{Nd}_2\text{Fe}_{14}\text{B}$ has Curie temperature around 250°C , which leads to limit its practical operating temperature under 150°C . Above the Curie temperature, the maximum energy product $(\text{BH})_{\text{max}}$ decline quickly to only 10% of its intrinsic $(\text{BH})_{\text{max}}$. [6] The coercivity decreasing problem of the $\text{Nd}_2\text{Fe}_{14}\text{B}$ can be improved by dysprosium [7]. By adding a small amount of dysprosium, the effective operating temperature of the $\text{Nd}_2\text{Fe}_{14}\text{B}$ magnet can be increased around 200°C . However, dysprosium is extremely expensive, and its attainability is not stable.

Rare earth crisis, which the demand for the RE materials surpassed the supply RE, has endangered the industries related to RE based permanent magnet. In 2002, Mountain Pass mine, the finest rare earth mine in the United States, stopped producing rare earth because of strict regulations and the high environmental cost. In consequence, China became the dominant rare earth supplier and succeeded in monopolization of rare earth element [8]. As the demand for the rare earth increase in domestic industries in China, the Chinese government has stringent the exporting regulation of rare earth materials. The acquiring enough amount of neodymium for electrical vehicles is becoming challenging. In addition, dysprosium is scarce. About 45K tons of neodymium magnets are produced in 2010 along [8], and it will be increased as the number of the electric cars are multiplies each year. Mining and the refining of the rare earth elements also involve costly processes and produce radioactive waste such as uranium contaminated soil and liquid.

In this regard, development of rare-earth-free magnets, which are not necessarily over performing RE-based magnets, but could replace RE-based magnets in a wide range of applications, is important for many industries. Several different approaches

have been explored to produce RE-free magnets. Reducing the size of the magnetic particles to the size of single magnetic domain size been proposed and demonstrated [3].

One of the efforts to develop rare earth free magnets, exchange-spring magnets which is an artificial composite of the hard and soft phase of magnets suggested by Kneller and Hawig [9] is considered to be the most promising method to produce rare earth free magnet. The principle of exchange spring magnet is that hard phase magnet and soft phase magnet interact at the interface so that hard phase magnetic material provides high coercivity while soft phase enhances the overall magnetization [10].

Spring magnet has been demonstrated by the epitaxial growth of SmCo/Fe and SmCo/Co. [11, 12]. Also, a recent report claimed that $(BH)_{\max} \sim 50\text{MGOe}$ was achieved by epitaxially grown FePt/FeCo[1]. However, an epitaxial growing method is not suitable for practical manufacturing. Because of extremely slow processing rate, high process cost and difficulty of expanding the apparatus to production scale. While much effort is focused on the multi-layered structure by epitaxial growth, theoretical modeling suggests nanocomposite approach is more realistic and have higher potential to achieve high $(BH)_{\max}$ [13].

Among many permanent magnets explored, MnBi permanent magnet has suggested as a promising material for hard phase magnet that could be used as the core of the exchange coupled spring magnet. MnBi is unique material that has positive temperature coefficient for magnetic coercivity. Its coercivity reaches a maximum at around 540K. In order to achieve high coercivity in permanent magnet, high magnetic anisotropy is preferred [1] MnBi has NiAs-type hexagonal structure, and its hexagonal c/a ratio changes from 1.425 to 1.433 gradually as temperature increase [14, 15].

The core-shell structure is one of the possible manufacturable forms of exchange coupling spring magnet and demonstrated by many researchers [16]. The core-shell structure also provides additional advantages. The material in the core is protected from oxidation by the shell structure [17, 18]. MnBi, one of the most attractive hard phase magnets for spring magnet, in nanostructured form is vulnerable for oxidation. Coating MnBi nano or submicron particles with soft magnets such as Co or FeCo would protect MnBi from oxidation but also results in exchange coupling.

The most of the core-shell structure was achieved by either wet chemical process or oxidation of the outer surface of the core materials [16]. However, forming a core-shell structure by these conventional methods is difficult for most of magnetic materials. In this paper, we present an experimental demonstration of a noble approach to form core-shell structure by sonic agitation assisted PVD deposition (SAA-PVD).

3.2 Experimental method

3.2.1 Preparing ballmilled MnBi particles

LPT-MnBi ingots (99%) were purchased from ACI ALLOYS, INC. The ingots were roughly cut into 1cm^3 , and one piece was put into an O-ring sealed aluminum container with argon gas and 2mm diameter ceramic balls. All materials were handled in a glove box that has less than 5 ppm oxygen contained argon atmosphere. The aluminum container mounted on a commercial SPEX mill and milled for 24hours. The milled particles were characterized with SEM and VSM first. In order to prevent oxidation of the MnBi particles during VSM measurement, the powders were encapsulated in aluminum specially shaped foils and sealed by deformation of the foil. The B-H hysteresis loop was measured by VersaLabTM VSM.

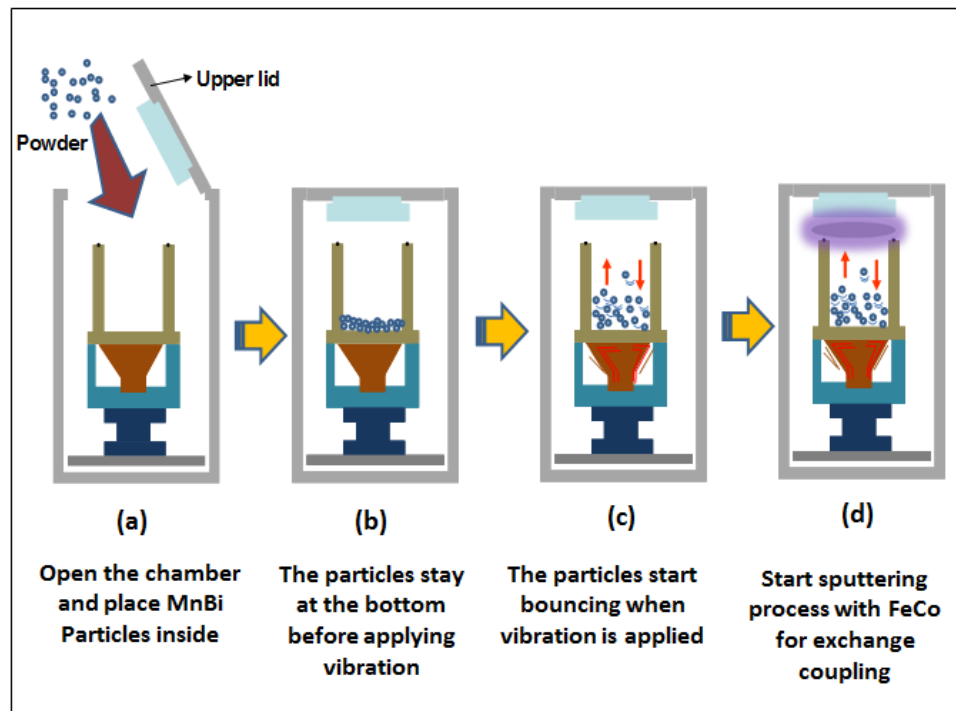


Figure 3.1 The concept of the sonic agitation assisted particle sputtering.

Experimental setup of SAA-PVD

The principle of the Sonic-agitation assisted PVD was explained in Figure 3.1. PVD on stationary particles would cause the particles embedded in the thin film. However, the sonic agitation would cause the particles randomly move and rotate, hence, the coating material would form a shell on a particle. The 100hz ultrasonic transducer was used to apply vibration. The power of the alternate current was applied through the commercial feed through.

Figure 2. shows the Schematics of the SAA-PVD system. The system consists of the piezoelectric transducer and particle pot that has thin (~10mil thick) bottom wall. The pot is attached to the piezoelectric base by spring loaded pins as shown Figure 3.2.

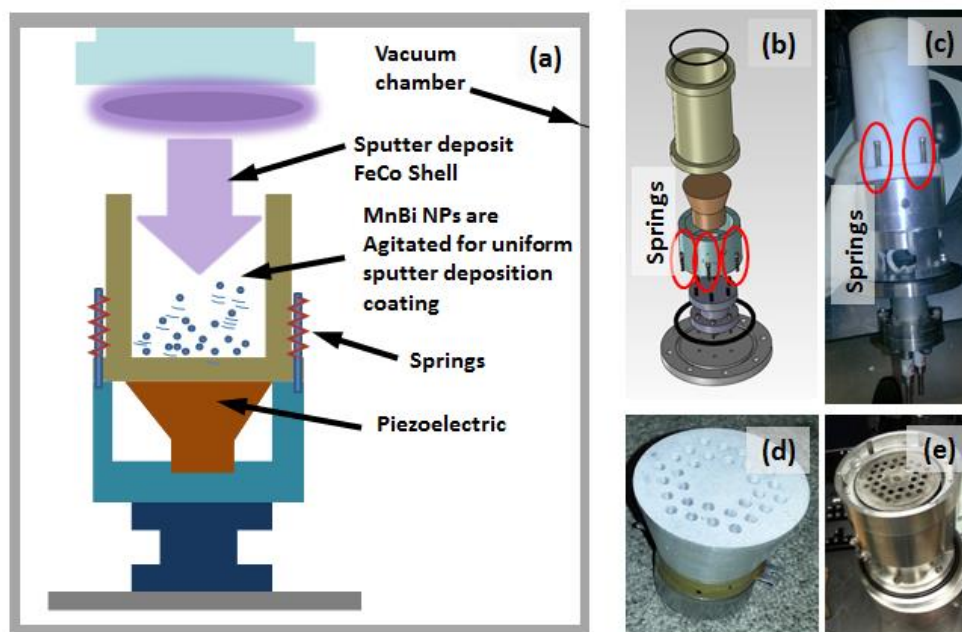


Figure 3.2 The structure of the Sonic agitation assisted particle sputtering system. (a) Schematics of SAPVD system. (b) Schematics of the vibration stage. (c) Photograph of the vibration stage. (d) The piezoelectric block (e) Assembly of piezoelectric base.

(b and c). The preloaded compression of the spring was precisely adjusted while monitoring the movement of the particles with a temporary viewport. The optimized particle's movement was depicted in Figure 3.5 (c).

MnBi nanoparticles are vulnerable to oxidation. Thus special design is required to prevent particles exposed to oxygen. Vacuum feed-through type manipulators were utilized to open the lid of the particle compartment in the vacuum chamber as shown in Figure 4. The manipulator shaft shown in the can move back and forth and can rotate. During the movement of the manipulator, the level of the vacuum in the chamber does not change from the $\sim 2.0 \times 10^{-5}$ Torr.

Particles were loaded in an o-ring sealed compartment as shown in Figure 3.4

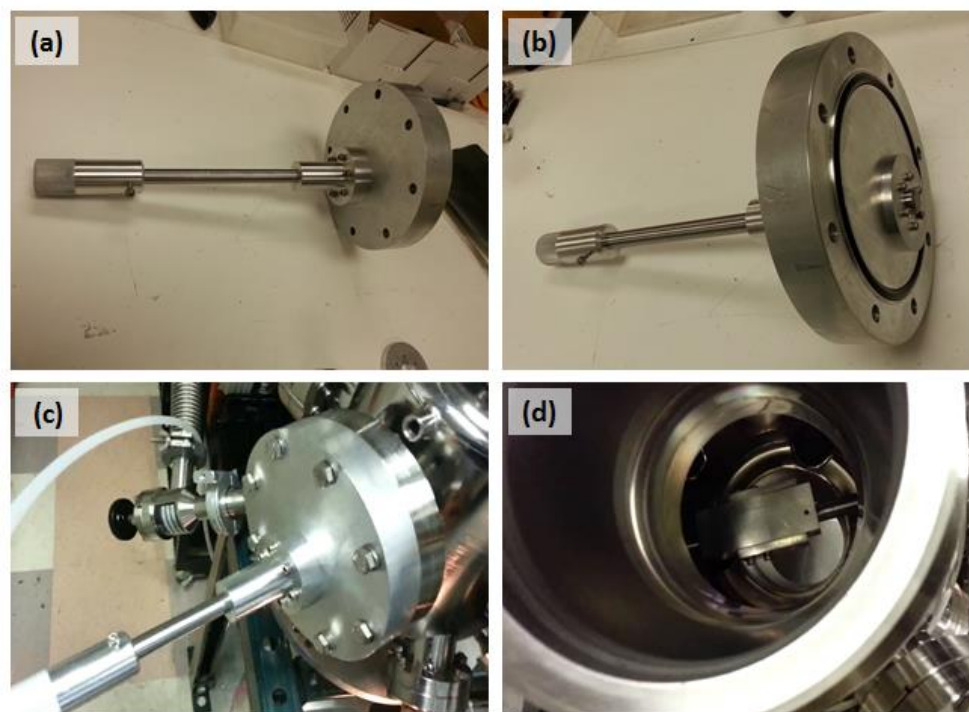


Figure 3.3. The photographic image of vacuum feed through manipulator (a and b) The image of the manipulator front and back. (c) The manipulator on the sputtering chamber. (d) the connection between the manipulator and the compartment.

and mounted on the shaft of the manipulator in a vacuum chamber as shown in Figure 3.3 (d). The O-ring slides into the gap between the upper and the bottom of the plate as shown in Figure 3.3 (a and b). The round corner of the upper plate prevents damaging of the o-ring during the sliding movement. Also, tiny amount of Dow Corning 976V High vacuum Silicon grease was applied on the o-ring. Deformation of the o-ring is about 20% of its original thickness when the compartment is completely closed. The sealing was adequate enough to protect MnBi particles from oxidation when the compartment was taken out from the argon filled glove box. The compartment was opened in the vacuum chamber when the pressure of the chamber was blown 2.0×10^{-5} Torr by manipulator described above.

Particles loaded in the compartment were drop to the vibrating pot by rotation of the manipulator, which flips over the compartment upside down, in a vacuum. The compartment moves away towards the outer side of the chamber after pouring out the particles into the vibrating pot so that the compartment and the manipulator do not block the sputter gun.

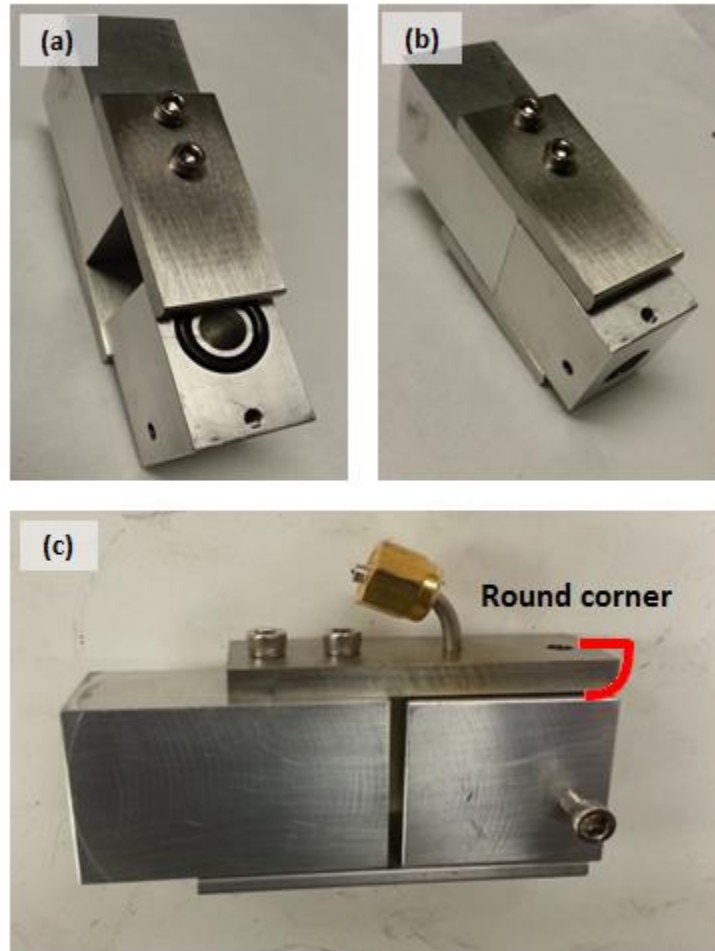


Figure 3.4 The image of the particle carrying compartment (a) when the compartment is open. (b) when the compartment is closed. (c) The side image.

The overview picture of the SAPVD is depicted in Figure 3.5 (a). when ultrasonic is applied to the thin bottom wall, the particles are highly mobilized as shown in Figure 3.5 (c). Sputtering started 30 seconds after the vibration started so that slight agglomeration broke and agitated particles form clouds as shown Figure 3.5 (c). During the deposition, the pressure in the chamber was maintained at 5mTorr by flowing

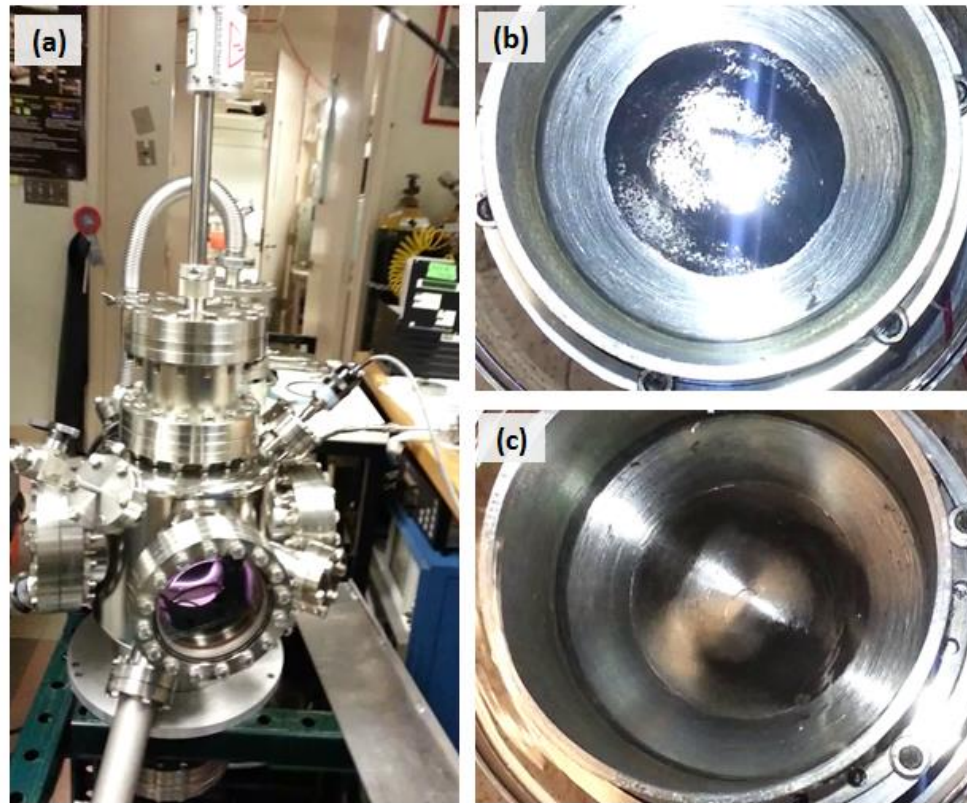


Figure 3.5. The photograph of the sputtering chamber and ultrasonic vibrating pot. (a) overview of the chamber. (b) Stationary particles in the vibrating pot before ultrasonic is applied. (c) Vibrating particles in the pot after ultrasonic is applied. The motion of the particles was observed by temporary viewport.

50sccm of argon gas. AJA sputtering gun was utilized, and Dc power 150W was applied on $\text{Fe}_{50}\text{Co}_{50}$ target.

After 90 seconds of FeCo deposition, the particles were collected with argon gas flushing. The opening of the chamber and the time was minimized, and the top of the vibrating top was immediately closed with o-ring sealed cap.

3.3 Result and discussion

3.3.1 Magnetic properties

Noble particle deposition process has been demonstrated. As shown in Figure 3.7, the magnetization of ball milled MnBi particles has increased by nearly 100% while only slight decrease in H_c was observed. Ball-milled powder has $M_s = 36$ emu/g and $H_c = 1.1$ T. The powder after the sonic-agitation assisted PVD process the M_s of the particle was increased 51 emu/g at $H = 3$ T and H_c was =1T. the enhancement of the magnetization is calculated to be 40%. The increase of magnetization accompanied by a

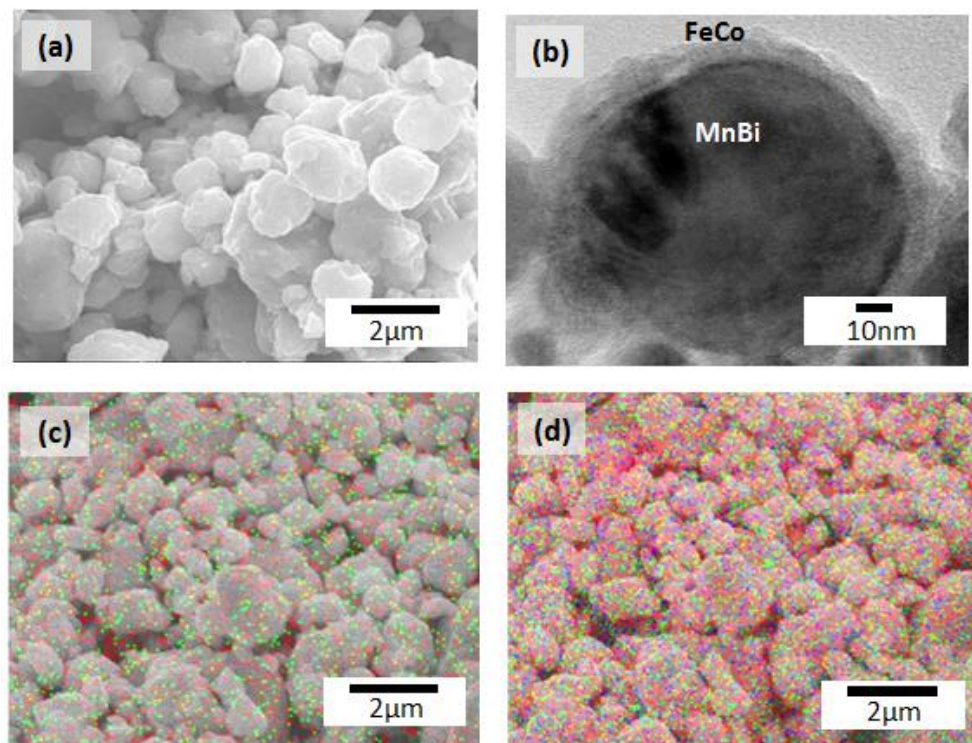


Figure 3.6 Image of the MnBi particles (a) SEM image after ball milling process (b) TEM image after SAPVD process (c) SEM image of particles after SAPVD process with FeCo EDX mapping. (d) SEM image of particles after SAPVD process with MnBi EDX mapping.

decrease of H_c is commonly observed in exchanged coupling [16].

3.3.2 Exchange coupling

One of the important indications for exchange coupling is the shape of the demagnetization curve. As shown Figure 3.7, the FeCo and MnBi has an extreme difference in their coercivity. If those two materials are simply mixed without exchange coupling, the huge magnetic hardness difference would have cause a constricted M-H loop [9]. Smooth demagnetization curve in the M-H loop of SAA-PVD processed particle, which is similar to the original shape of hard phase core, suggests exchange coupling between hard and soft phase possibly achieved.

The size of the MnBi particles after the ball milling process was range between 200nm and 2 μ m as shown in Figure 3.6 (a). Theoretical single domain size of MnBi is reported as the range between 0.33 μ m and 0.52 μ m [19]. However, experimentally confirmed single domain size is more likely 1 μ m [20]. The discrepancy between the theoretical value and experimental value is due to the fact that the theoretical calculations used Block-wall energy density σ_w obtained from MnBi thin films which could be different in particles [20]. Therefore the size of the ball-milled particles are within twice of single domain 2δ which is optimal size of hard phase for exchange coupling.

The TEM image in Figure 3.6 (b) shows solid MnBi particle in the center and a thin layer of FeCo on the shell. The thickness of the shell is in the range of 10 ~ 35 nm. EDX mapped image after SAPVD process also shows uniform deposition of FeCo layer on the MnBi particles. A single domain of FeCo is range between 14~70nm [21]. The

thickness of the FeCo layer in is less than the optimal size of $2\delta_s$ (twice of single domain size of soft magnetic phase).

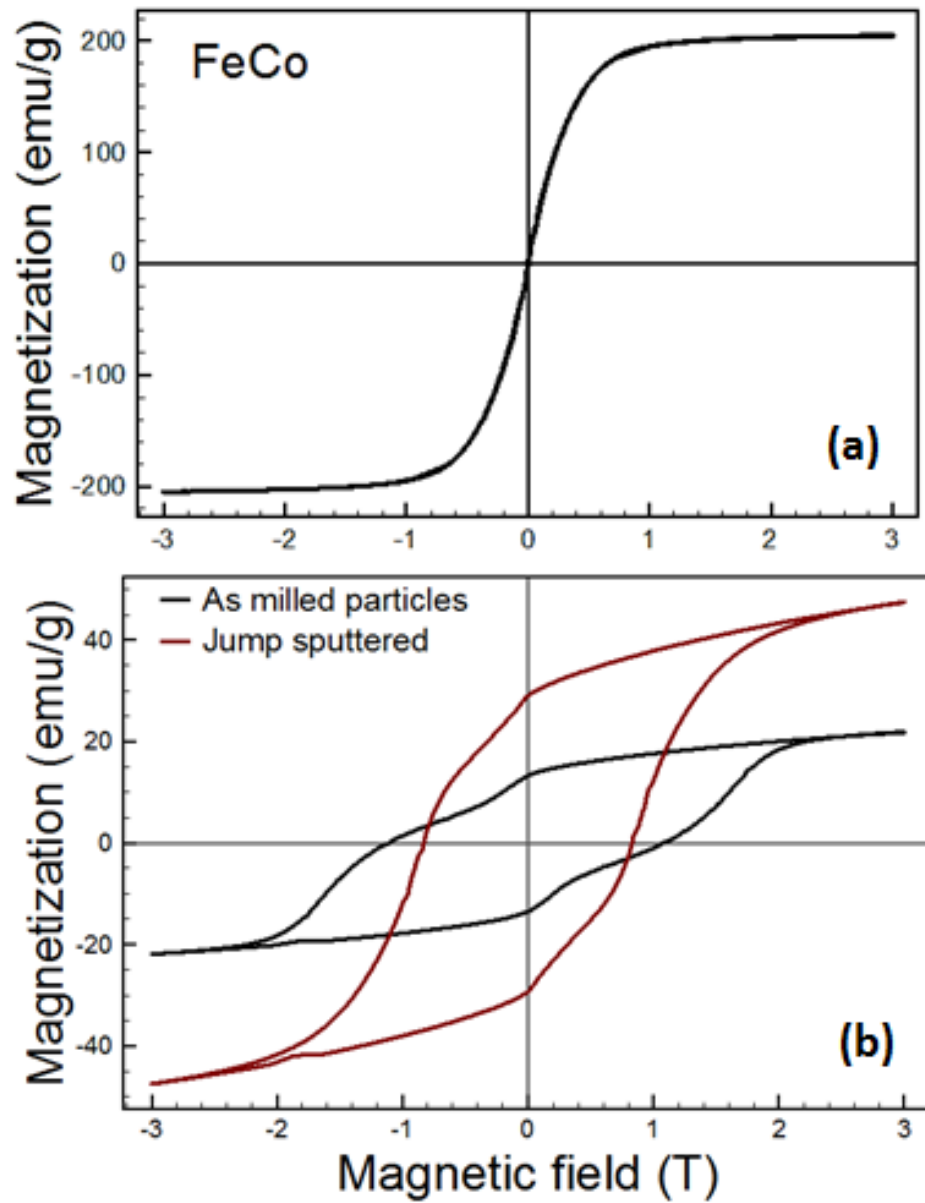


Figure 3.7 M-H loop measurement of (a) FeCo particles (b) Ball milled MnBi (black) and After SAPVD process (Red).

The coercivity of Bulk MnBi is close to zero [22] or about ~30 Oe. As the size of the particle decrease, coercivity increases. The maximum coercivity can be achieved when the size of the particle is less than the size of the single domain. The size of our ball milled sample is close to 1~2 domain size, therefore the close to 1.1T coercivity can be explained by the size of the particles.

The magnetization of the ball-milled particles was about 36 emu/g, which is much lower than 70emu/g magnetic remanence of bulk MnBi. The low saturation magnetization value could be caused decomposition of MnBi and damage of crystalline structure during the ball milling process. Similar remanence also has been observed in similar ball milling process [23].

There is a possibility that the magnetization remanence enhancement could be attributed annealing effect. In this case, significant decreasing of coercivity also observed. However, the high increase of magnetic remanence observed after SAA-PVD process is hard to be related annealing effect during the process. The deposition time is only 90 seconds, and the distance of the plasma region and the particles is about 15cm. The only slight coercivity decrease also suggests that the high increase of the magnetic remanence is more likely due to the exchange coupling.

Due to the low saturation magnetization before the SAPVD process, the value of the saturated magnetization is only 51 emu/g despite 100% increase of saturation. H_{ci} is larger than $B_r/2$ therefore $(BH)_{max}$ calculated by $(B_r)^2/4$ [24]. Using density of MnBi particles 8.4g/cm^3 [23, 25], the calculated $(BH)_{max}$ of the particles are about 2.5MGOe.

3.3.3 Feasibility of SAA-PVD process

SAA-PVD system has several advantages on producing core-shell structures. Unlike chemical process, the shell material does not form segregated independent particles. Uncoupled FeCo particles would cause two-phase magnetic behavior. The shell material cannot form a particle in SAPVD process since the arriving atoms only bind with existing surface. The random movement of agitated MnBi particles increases the chance to meet the new arriving atoms, and few atoms that impact the wall of the vibrating pot before encounter MnBi particles will grow as a continuous film on the wall which does not mix with core-shell structured particles.

Strong adhesion through SAA-PVD could increase the exchange coupling. PVD process utilized the high momentum of atoms produced by a plasma process. Thus the atoms deposited on the particles impact the surface of the particles, and as a result newly arriving atoms can be embedded in few nanometers of the layer due to the kinetic energy. Slight oxidation could be overcome by these strong coupling.

SAA-PVD is suitable for larger scale process. Growing of particles from PVD process is technically difficult and expensive. However, depositing thin shell materials on particles reduces the processing time compare to producing particle without a large volume of core particles. Compared to the wet process, SAA-PVD does not require post processes. Collecting particles from wet process involves difficulty in separating particles from the working fluids. Also, contamination could be problematic.

Agitation due to 100 KHz also prevents agglomeration. SEM analysis shows individually separated particles rather than a large cluster. Conventional PVD deposition on stationary particles could produce bonding between adjacent particles.

However, the vibration and movement of particles prevent bonding caused by the coating material. The deposition rate was ~ 0.29 nm/s. The frequency of 100 KHz and 80 W power is sufficient enough. Moreover, a high degree of separation was observed after SAPVD due to ultrasonic vibration. The result is also in accordance with several reports that studied particles separation using sonication in wet processes [26, 27]. The power of the ultrasonic and the minimum size of agglomerate that can be broken down is not linear [26]. Also, there is an asymptotic limit that further increase of the power cannot reduce the size of agglomerates due to the strong adhesion force between small particles [27].

Wet process cannot be used oxidation-sensitive materials such as MnBi. The SAA-PVD process is mostly done in inert gas such as Ar or in vacuum. Therefore, the process is free from oxidation. The sample handling technique introduced in this study is proved to be efficient. The detail about the particle carrier compartment is also discussed in the experimental section. The shell materials that produced through SAA-PVD can protect the core materials. FeCo has much low oxidation

3.4 Conclusion

Exchange spring magnet using MnBi hardcore and FeCo soft shell has been demonstrated. The size range of the MnBi particles by ball milling was between 200 nm and 2 μ m. Most of the particles were within the optimal size of hardcore that is 2δ (twice of single domain size of a hard magnet). The shell produced by SAA-PVD process was about 10 ~ 35 nm which is slightly less than 2δ s. Ball-milled powder had $M_s = 36$ emu/g and $H_c = 1.1$ T. The powder after the SAA-PVD process, the M_s of the particle, was increased 51 emu/g at $H=3$ T and H_c was = 1T. The $(BH)_{max}$ of the particles after the SAPVD process was about 2.5MGOe. The low $(BH)_{max}$ value was attributed to the low magnetization of the ball-milled particles. In order to achieve higher $(BH)_{max}$, decreasing of the magnetization during the ball milling process must be overcome. The concept of SAPVD was well demonstrated. Throughout EDX and TEM the shell material was well deposited on the core material. This demonstrated technique can be directly applied to other applications such as producing a core-shell structure for oxidation-sensitive materials. Co-deposition of several materials also could be possible so that alternating multilayers of the soft magnet and hard magnet could be materialized.

3.5 References

1. Giannopoulos, G., L. Reichel, A. Markou, I. Panagiotopoulos, V. Psycharis, C. Damm, S. Fähler, I. Khan, J. Hong, and D. Niarchos, *Optimization of L10 FePt/Fe45Co55 thin films for rare earth free permanent magnet applications*. Journal of Applied Physics, 2015. **117**(22): p. 223909.
2. Gutfleisch, O., M.A. Willard, E. Brück, C.H. Chen, S. Sankar, and J.P. Liu, *Magnetic materials and devices for the 21st century: stronger, lighter, and more energy efficient*. Advanced materials, 2011. **23**(7): p. 821-842.
3. López-Ortega, A., E. Lottini, C.d.J. Fernandez, and C. Sangregorio, *Exploring the magnetic properties of cobalt-ferrite nanoparticles for the development of a rare-earth-free permanent magnet*. Chemistry of Materials, 2015. **27**(11): p. 4048-4056.
4. Sagawa, M., S. Hirosawa, H. Yamamoto, S. Fujimura, and Y. Matsuura, *Nd-Fe-B permanent magnet materials*. Japanese journal of applied physics, 1987. **26**(6R): p. 785.
5. Strnat, K., *The recent development of permanent magnet materials containing rare earth metals*. IEEE Transactions on Magnetics, 1970. **6**(2): p. 182-190.
6. Hong, Y.-K., J. Park, O.N. Mryasov, S.-G. Kim, S. Kim, J. Lee, G.S. Abo, C.-J. Choi, and J. Lee, *Magnetic properties of MnBi based alloys: First-principles calculations for MnBi-Co and MnBi-Co-Fe cases*. AIP Advances, 2013. **3**(5): p. 052137.
7. Pathak, A.K., M. Khan, K.A. Gschneidner, R.W. McCallum, L. Zhou, K. Sun, K.W. Dennis, C. Zhou, F.E. Pinkerton, and M.J. Kramer, *Cerium: an unlikely replacement of dysprosium in high performance Nd-Fe-B permanent magnets*. Advanced Materials, 2015. **27**(16): p. 2663-2667.
8. Takeda, O. and T.H. Okabe, *Current status on resource and recycling technology for rare earths*. Metallurgical and Materials Transactions E, 2014. **1**(2): p. 160-173.
9. Kneller, E.F. and R. Hawig, *The exchange-spring magnet: a new material principle for permanent magnets*. IEEE Transactions on Magnetics, 1991. **27**(4):

p. 3588-3560.

10. Jiang, J., J. Pearson, Z. Liu, B. Kabius, S. Trasobares, D. Miller, S. Bader, D. Lee, D. Haskel, and G. Srajer, *A new approach for improving exchange-spring magnets*. Journal of applied physics, 2005. **97**(10): p. 10K311.
11. Fullerton, E.E., J.S. Jiang, and S.D. Bader, *Hard/soft magnetic heterostructures: model exchange-spring magnets*. Journal of Magnetism and Magnetic Materials, 1999. **200**(1–3): p. 392-404.
12. Davies, J.E., O. Hellwig, E.E. Fullerton, J. Jiang, S. Bader, G. Zimanyi, and K. Liu, *Anisotropy dependence of irreversible switching in Fe/SmCo and FeNi/FePt exchange spring magnet films*. Applied Physics Letters, 2005. **86**(26): p. 262503.
13. Liu, X., S. He, J.-M. Qiu, and J.-P. Wang, *Nanocomposite exchange-spring magnet synthesized by gas phase method: from isotropic to anisotropic*. Applied Physics Letters, 2011. **98**(22): p. 222507.
14. Yang, J., Y. Yang, X. Chen, X. Ma, J. Han, Y. Yang, S. Guo, A. Yan, Q. Huang, and M. Wu, *Anisotropic nanocrystalline MnBi with high coercivity at high temperature*. Applied Physics Letters, 2011. **99**(8): p. 082505.
15. Heikes, R., *Magnetic transformation in MnBi*. Physical Review, 1955. **99**(2): p. 446.
16. Imaoka, N., E. Kakimoto, K. Takagi, K. Ozaki, M. Tada, T. Nakagawa, and M. Abe, *Exchange coupling between soft magnetic ferrite and hard ferromagnetic Sm₂Fe₁₇N₃ in ferrite/Sm₂Fe₁₇N₃ composites*. AIP Advances, 2016. **6**(5): p. 056022.
17. Li, Y., S. Ji, Y. Gao, H. Luo, and M. Kanehira, *Core-shell VO₂@TiO₂ nanorods that combine thermochromic and photocatalytic properties for application as energy-saving smart coatings*. Scientific reports, 2013. **3**.
18. Gao, Y., S. Wang, H. Luo, L. Dai, C. Cao, Y. Liu, Z. Chen, and M. Kanehira, *Enhanced chemical stability of VO₂ nanoparticles by the formation of SiO₂/VO₂ core/shell structures and the application to transparent and flexible VO₂*

based composite foils with excellent thermochromic properties for solar heat control. Energy & Environmental Science, 2012. **5**(3): p. 6104-6110.

19. Kishimoto, M. and K. Wakai, *Single-domain properties in MnBi particles.* Japanese Journal of Applied Physics, 1976. **15**(9): p. 1843.
20. Munakata, M., K. Goto, and T. Sakurai, *Magnetic domain studies on single-domain particles of the low-temperature phase of MnBi by the colloid-SEM method.* Philosophical Magazine Part B, 1983. **47**(4): p. 431-436.
21. Hesani, M., A. Yazdani, B.A. Ravan, and M. Ghazanfari, *The effect of particle size on the characteristics of FeCo nanoparticles.* Solid State Communications, 2010. **150**(13): p. 594-597.
22. Nguyen, P.-K., S. Jin, and A.E. Berkowitz, *MnBi particles with high energy density made by spark erosion.* Journal of Applied Physics, 2014. **115**(17): p. 17A756.
23. Nguyen, V.V., N. Poudyal, X.B. Liu, J.P. Liu, K. Sun, M.J. Kramer, and J. Cui, *Novel processing of high-performance MnBi magnets.* Materials Research Express, 2014. **1**(3): p. 036108.
24. Xu, X., Y.-K. Hong, J. Park, W. Lee, A.M. Lane, and J. Cui, *Magnetic self-assembly for the synthesis of magnetically exchange coupled MnBi/Fe–Co composites.* Journal of Solid State Chemistry, 2015. **231**: p. 108-113.
25. Zhang, D., S. Cao, M. Yue, W. Liu, J. Zhang, and Y. Qiang. *Study on bulk nanostructured MnBi permanent magnet prepared by spark plasma sintering.* in *APS Northwest Section Meeting Abstracts.* 2010.
26. Taurozzi, J.S., V.A. Hackley, and M.R. Wiesner, *Ultrasonic dispersion of nanoparticles for environmental, health and safety assessment – issues and recommendations.* Nanotoxicology, 2011. **5**(4): p. 711-729.
27. Bihari, P., M. Vippola, S. Schultes, M. Praetner, A.G. Khandoga, C.A. Reichel, C. Coester, T. Tuomi, M. Rehberg, and F. Krombach, *Optimized dispersion of nanoparticles for biological in vitro and in vivo studies.* Particle and Fibre Toxicology, 2008. **5**(1): p. 14.

Chapter 4. Thermochromic Vanadium Oxide Film by Thermal decomposition method

4.1 Introduction

The amount of natural resources such as fossil fuel including coal, natural gas, and petroleum is finite while the global consumption of these rapidly increasing. Much research effort has focused on the development of renewable energy production, however, without effort to save energy and other finite resources, energy shortage problem could be imminent. The sectors that have the largest potential to reduce the energy use are residential areas, and the office buildings since in most of countries more than 40% of energy is consumed for heating, cooling and lighting in these sectors [1, 2].

Controlling the amount of energy entering buildings using thermochromic smart window based on vanadium dioxide (VO_2) has been suggested to as one of the effective solutions to save energy [3]. VO_2 (M), one of many polymorphic forms of vanadium oxide, exhibits a fully reversible semiconductor-metal phase changing property depends on temperature. Below the critical temperature T_c , which defined by the temperature that MIT transition occurs, VO_2 exhibits the properties of semiconductors. At a temperature above the T_c , VO_2 shows the properties of metal. [4].

Although VO_2 (M) phase is a promising thermochromic material that has huge potential to save energy, scalable synthesis method has not been successfully developed yet. In this regard, new methodologies are still worthy to be explored for a large quantity of production [5]. The biggest difficulty of synthesizing thermochromic vanadium is achieving the exact stoichiometry and phase of vanadium oxide that exhibit MIT transition. Vanadium oxide has a very complex phase system. There are several

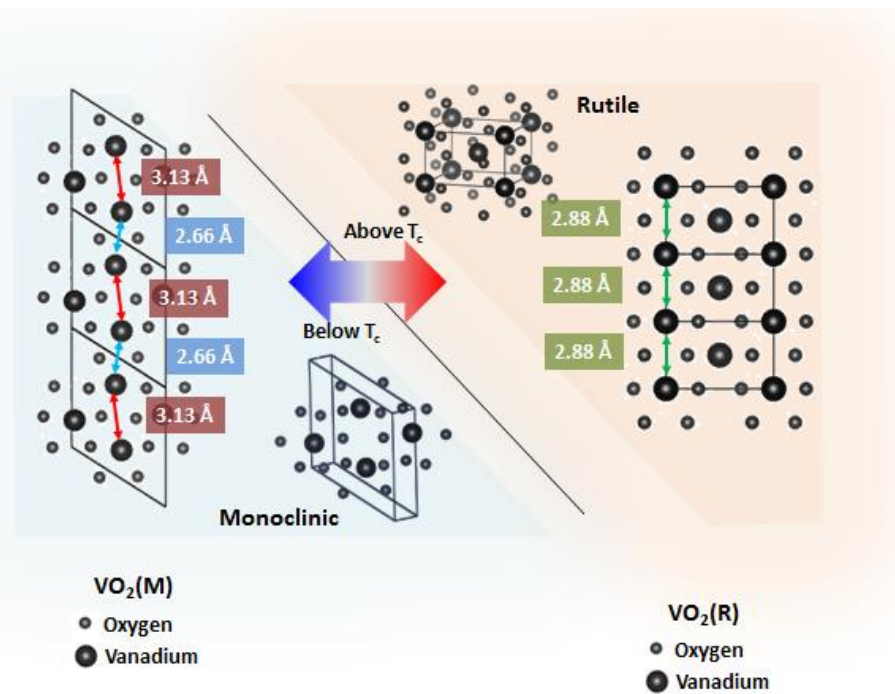


Figure 4.1 Crystalline structure change of VO₂(M) depends on the temperature stoichiometric forms of oxides such as V₂O₃, VO₂, V₄O₇, V₅O₉, V₆O₁₁, V₇O₁₁, V₃O₄ and V₂O₅. Even VO₂ has several polymorphic such as VO₂ (A), VO₂ (B), VO₂ (D), and VO₂ (M), and the VO₂ (M), the desirable phase for thermochromic application, can be obtained in very narrow condition.

In previous decades, gas phase based method such as PVD and CVD has been utilized to obtain VO₂. However, these methods are too costly for practical use also it is difficult to deposit large area using these methods.

Many different synthesis methods such as hydrolysis [4], hydro thermal[6], and sol-gel processes have been studied. Some of the VO₂ synthesis methods take very long time and complicated processes. VO₂(R) powder by the hydrothermal treatment of V₂O₅ and H₂C₂O₄ at 240 C for 7 days. Some of the synthesis methods only produced either

VO₂ (A) or VO₂ (B) phase, or a small portion of M1/R phase with non-uniform morphologies. Few scalable approaches such as spray pyrolysis have also been tried without a successful result. The XRD peak of the obtained particles presented in the report shows the low purity of VO₂ (M) phase [7].

Embedding VO₂ (M) particles in polymer matrixes has been suggested as a more realistic approach to preparing a thermochromic film with a large area with the assumption that adequately scalable particle synthetic process can be developed near future. Contrary to the gas vapor deposition, the mixture of the VO₂ (M) powder and polymer could be cast on any size of the area by casting method. Imbedding particles in polymer matrices also has other advantages. VO₂ (M) particles can be prepared on the substrate that has low thermal endurance such as polymer film by a casting method. Formation of VO₂ (M) requires a high-temperature process such as hydrothermal and annealing. However, embedding methods provide the means to separate film preparation process from high-temperature processes. VO₂ (M) particles can be prepared in the conventional process, and then later mixed in a polymer matrix at low temperature [5].

The polymer matrix also prevents the VO₂ particles from oxidation and increase the stability of it [4]. VO₂ is only a metastable phase among complicated VO₂ phase system, and easily transformed into V₂O₅ when it is exposed to the air for a long time. In order to increase the stability of VO₂ nanoparticles SiO₂/VO₂ core-shell and structure and TiO₂/VO₂ core-shell also has been explored[2, 8]. However, the core-shell process requires costly extra steps, and cracking of the shell structure could also be potential problems. Few images in the report show the cracking of the shell structure [2].

Polymer matrix, in contrast to the hard SiO₂ or TiO₂ shell, provides protection from the oxidation without cracking.

The criteria of the practical applications for the VO₂ film are exceeding 40% T_{lum} and exceeding 10% of ΔT_{sol} . T_{lum} is defined by transmittance of visible light, and can be determined by $T_{lum} = \int \varphi_{lum,sol} T_{(\lambda,\tau)} d\lambda / \int \varphi_{lum,sol} d\lambda$. ΔT_{sol} is defined by difference between transmittance of entire range at low temperature and high temperature, and can be determined by $\Delta T_{sol} = T_{lum(\tau < T_c)} - T_{lum(\tau > T_c)}$ where φ_{lum} is the spectral sensitivity of the light-adapted eye and φ_{sol} is the solar irradiance spectrum of an air mass of 1.5 [9, 10].

The transmittance and the solar energy modulation ability of the film mainly depend on the thickness of the VO₂ film. Kang et al. have shown that the thickness of the VO₂ film above ~ 100nm, T_{lum} decrease under 40%, while delta ΔT_{sol} increase as the thickness of the film increased [10].

4.2 Experimental method

4.2.1 Particle synthesis

VO₂ (M) particles are prepared by thermal decomposition method. 0.15mol of Oxalic acid (98%, Sigma Aldrich) and 0.01mol of vanadium (V) oxide (98%, Sigma Aldrich) was dissolved in 500mL of DI water and stirred for 10 hours. After the color was turned into transparent blue, the aqueous solution was dried by slow evaporation under reduced pressure. After the solution was completely dried, the obtained solid compound was finely ground by mortar and pestle. Before the annealing process, a small amount of the ground compound was analyzed with TGA. Rest amount of the ground compound was transferred into quartz crucibles and annealed in vacuum tubes for 3 hours. The annealing temperature each sample were 350°C, 400°C, 450°C and 500°C. The obtained powder was characterized by XRD, SEM, and other optical measuring units.

4.2.2 Tungsten doping

Ammonium metatungstate hydrate (99.99%, Aldrich) was added at the beginning of the VO₂(M) synthesis process so that a number of tungsten contents each solution became between 0 % and 2% of the amount of vanadium molarity in 0.5% interval.

4.2.3 Characterization of particles

The TGA study was performed to determine the effective range of the annealing temperature using Perkin Elmer Pyris 1 TGA. The temperature range for the test was between 50C and 900C, and the temperature increasing rate was 2.5 C/minutes.

Nitrogen gas was supplied 20ml/min. Weight change depends on the temperature was monitored with Pyris software. Throughout the result the complete decomposition temperature of the oxalic acid compound and the VO(CHO) compound. The XRD measurement was taken by Bruker D2 Phaser using CuK α radiation. The 2θ range was between 20 and 80 degrees and step size 0.014°. The XRD pattern was compared with JCPDS card #00-044-0252. Philips XL30 FESEM was used to analyze the morphologies of the particles at an acceleration voltage of 10KeV. Perkin Elmer DSC 8000 was used to determine the transition temperature of the VO₂ (M) samples.

4.2.4 Film preparing

VO₂ (M) particles were ball milled in four different conditions. 0.5 g of VO₂ powder was ball milled using 315g of alumina ball that has average size 3mm in diameter. Four different batches are ball milled with 800RPM for 80 min, 600RPM for 80 min, 400RPM for 80 min and 200RPM for 8min. After the ball milling process, the particles were characterized by XRD and SEM as described in characterization section. The ball-milled particles were separated by gravity in the following manner. 0.2g of ball milled VO₂(M) particles were mixed with 0.4g of PVP and 1g of Isopropanol alcohol and ultrasonic treated in a sonic bath for 10 hours. Light particles sustain colloidal states, but large particles were accumulated at the bottom of the solution. An only upper portion of the particles was taken and used for film preparation. The film was analyzed by SEM. The film was blade cast on the PET film with a 100 μ m guide.

4.2.5 Optical property characterization

The transmittance of the film was measured light wavelength between 200nm to 2500nm. After the transmittance of the film at low temperature was measured, the film was heated up to 80C, which is above the MIT Tc, using customized apparatus.

4.3 Result and discussion

4.3.1 Analysis on the particles

The annealing range of the vanadium oxide compound was determined based on TGA result. As shown in Figure 1. more than 90% of oxalic acid was 209C and nearly 100% of oxalic acid was decomposed around 270C. The TGA data of VO(CHO)

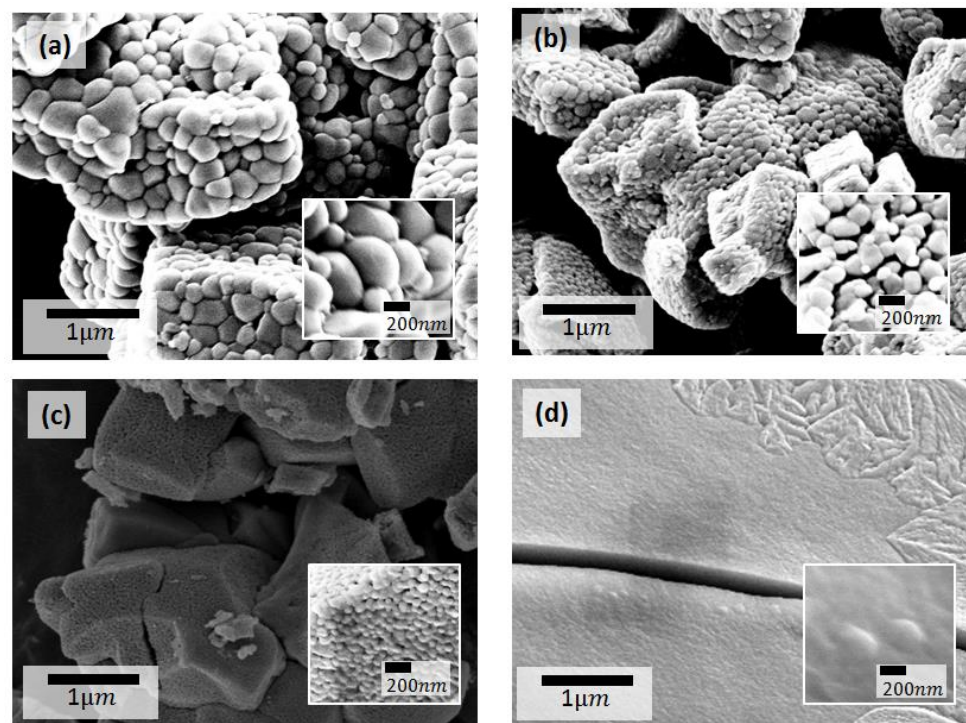


Figure 4.2 SEM images of the VO₂ particles annealed at (a) 500C (b) 450C (c) 400C (d) 350C for 3hours

compound shows about 25% of weight loss around 216C which could be attributed to the excess amount of oxalic acid in VO(CHO) compound. At 353C, VO(CHO) compound reached 60% of its original weight, and beyond 353C no further weight loss was observed. The weight loss of VO(CHO) between 216C and 353C could be attributed to slow decomposition of VO(CHO) into VO₂ and CO₂. Slight weight increase was observed between 350C and 800C which suggest that small amount of VO₂ was further oxidized due to the oxygen diffused from the outside chamber. The annealing range for the compound was determined to be 350C to 500C in 50C interval.

Figure 2 shows the XRD pattern of the annealed powders at different temperate. Except for the particle that was annealed at 350°C, all other particles have pure VO₂ (M) phase. The pattern of the particle annealed at 350°C shows nanocrystalline structure.

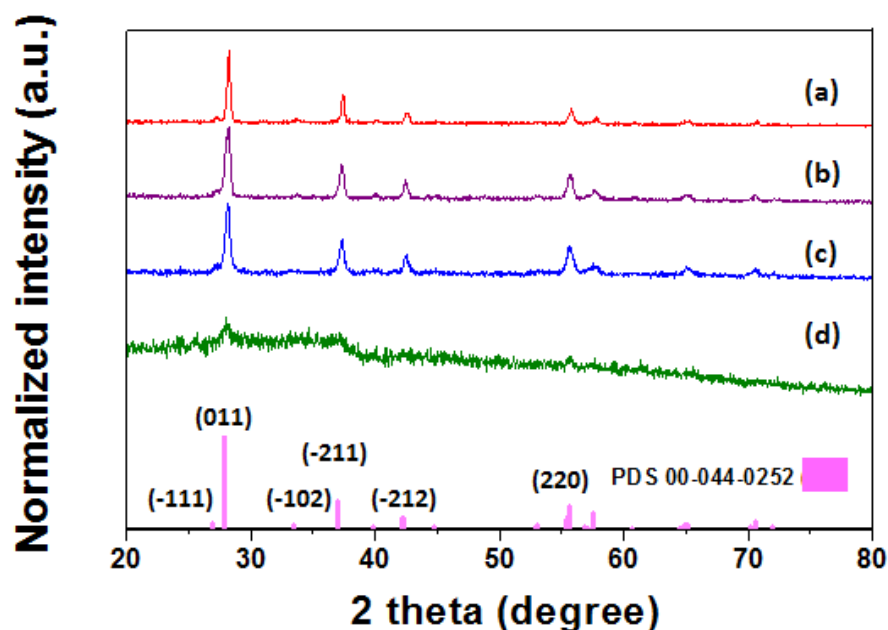


Figure 4.3 XRD pattern of VO₂ particles annealed at (a) 500 °C (b) 450 °C (c) 400 °C (d) 350 °C

The VO(CHO) compound annealed at possibly formed only amorphous structure. The size of the grains could be determined by HWHH of the main peak of each pattern. It shows that the particles annealed at 500°C have a grain size about 500 nm, particles annealed at 450°C has a grain size about 120 nm, and particles anneal at 400 °C has a grain size about 40 nm. SEM image in Figure 2. Shows consistent result. Fig 4.2 (a) shows the particles that have a size range between 400 nm and 600 nm slightly connected each other and makes clusters. The size of the clusters is about 1~2 μm. The best size for the thermochromic effect was particles around 100 nm as discussed in the previous section, in that regard, particles annealed at 400 °C was used selected to use ball milling and film preparation. The particle that was annealed at 450 °C has other advantages. When the particles were ball milled the particles can be divided into small sizes by breaking connections between the particles.

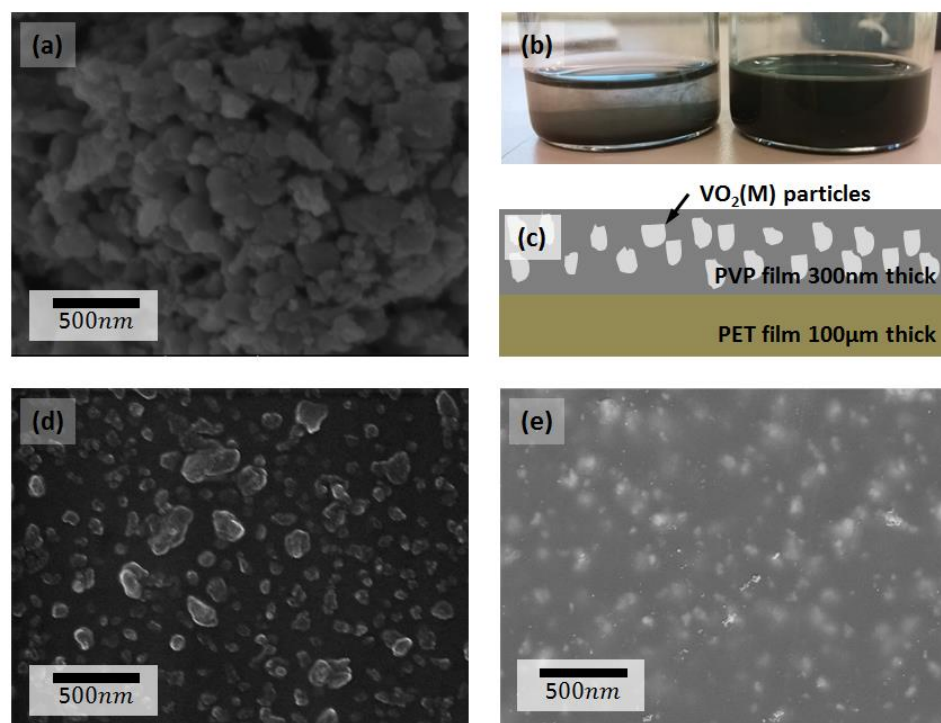


Figure 4.4 Image of ball milled particles and particles embedded in polymer matrix (a) SEM image of ball milled particles (b) VO₂ Particles dispersed by ultrasonic in IPA without PVP (right) and with PVP (left) (c) Configuration of the VO₂ particles embedded in PVP film (d) SEM image of dispersed VO₂ particles on a copper substrate (e) SEM image of VO₂ particles embedded in PVP film

The SEM images of the ball-milled particles are shown in Figure 4.4 as shown the size of the particles have a distribution between 20 nm and 200 nm. However, the percentage of the particle that exceeds 100 nm is small. When these large particles are embedded in the polymer matrix, few local ineffective spots can be created. The SEM image of the PVP film that VO₂ particles are embedded is shown in Figure 4.4. The particles are dispersed in the polymer matrix. The Thickness of the film that was measured with Dektak profiler was about 2μm. The thickness of the film and the

thickness of the guide might have discrepancy due to the low viscosity of the solution. After the blade casting the solution flow towards the edges while drying. Thus the center part of the film has a uniform thickness across 1inch^2 area however the thicker film was formed at the edges. The SEM image only shows the particles on the top of the films. However, the particles are dispersed in 3-dimensional spaces. Therefore, the projected coverage of the particles is close 100 % or even projection of some particles are overlapped. This configuration is more practical for commercialization. A continuous VO₂ film that has a thickness of 100nm or less is difficult to fabricate and expensive.

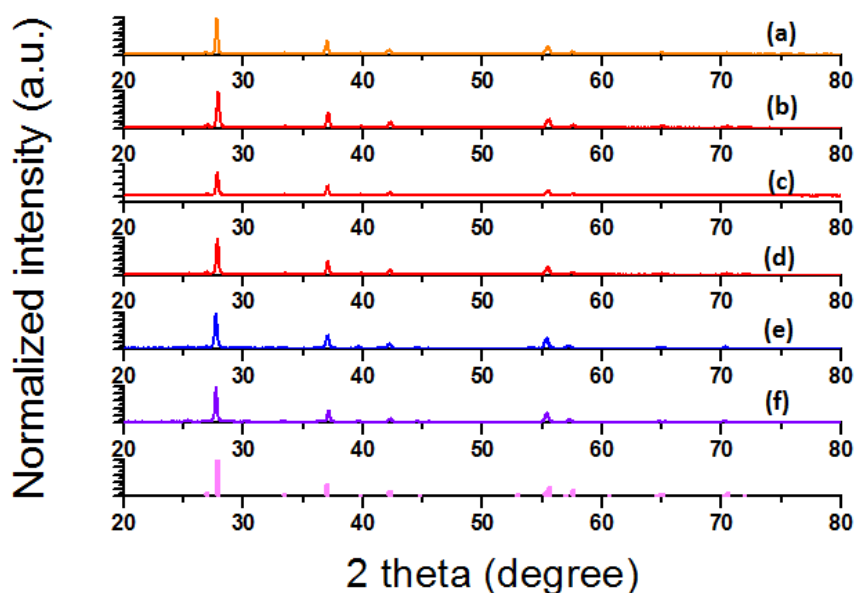


Figure 4.5 XRD patterns of VO₂ particles with tungsten concentration of (a) 0% (b) 0.5% (c) 1.0% (d) 1.5% (e) 2.0% (f) 2.5%. Peaks JCPDS #00-44-0252 is presented at the bottom.

4.3.2 IR modulation performance

Figure 4.7 shows the optical measurement of the VO₂ film. As shown, the transmittance of the Film in the visible range is slightly less than 40%, and the optical modulation is about 20%. The low transmission in the result could be attributed the particles that exceed 100nm and overlapping of the particles in the projected area. In order to increase the transmittance of the sample, the ratio of the VO₂ particles contained in the polymer or the thickness of the film should be reduced. The ratio between ball milled VO₂ particles and PVP was 1:2. Reducing the amount of the VO₂ particles would increase the transmittance of the visible range.

4.3.3 Controlling transition temperature

Figure 4.5 (a) shows the DSC result of samples doped with tungsten. The

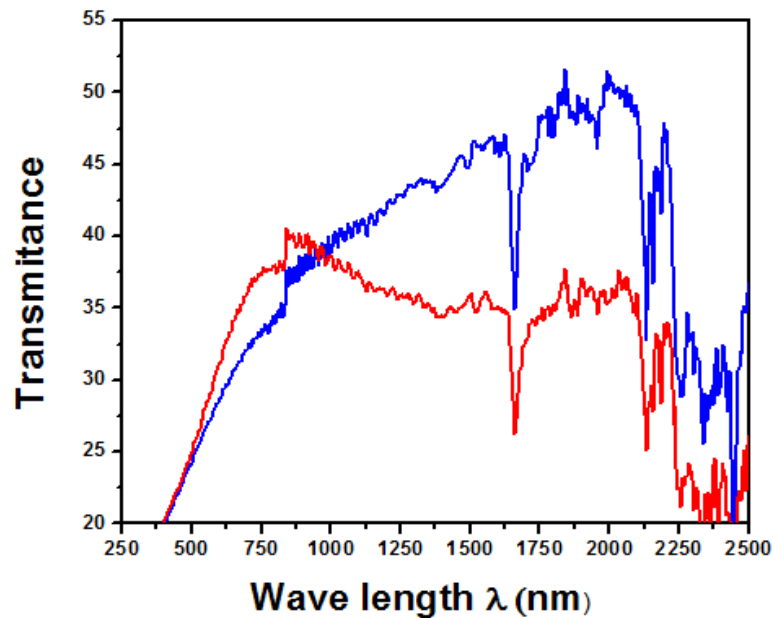


Figure 4.6 Optical measurement of the VO₂ embedded film at room temperature (blue) at 90 °C (red)

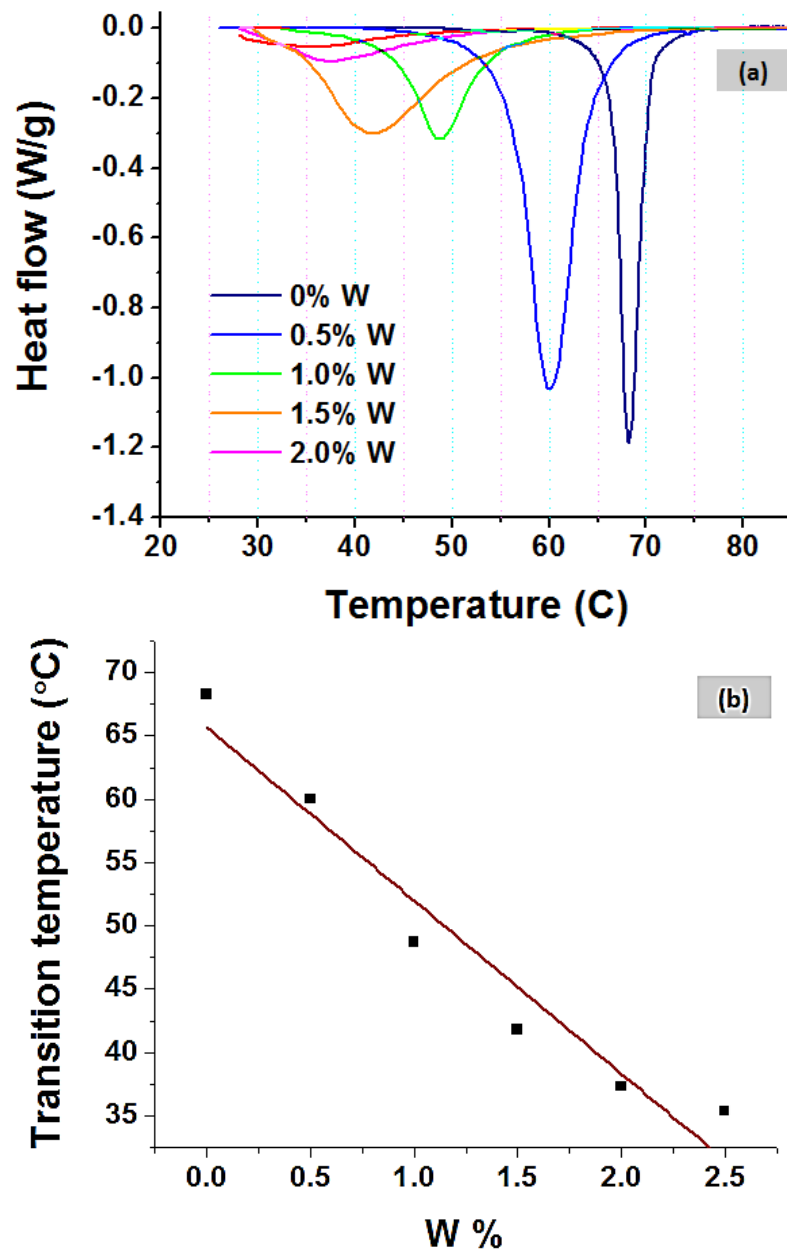


Figure 4.7 Change in transitioning temperature depends on percentage of tungsten doping (a) DSC curves of VO₂ particles with different W concentration (b) linear fitting of transition temperature change.

VO₂(M) without doping has transition temperature at 68°C degree same as other previous studies. The transition temperature changes of 13.6 °C/w% was observed as shown in the inset of Figure 4.5 (b). As the percentage of the doping increased the sharpness of the transition reduced. In order to confirm the crystalline structure of the doped particles, XRD pattern of doped samples was analyzed again. As shown in Figure 4.6, all of the samples has VO₂(M) phase. There was no sign of segregated tungsten oxide formation was observed. The decrease of the sharpness of DSC peak of doped VO₂ particles was often reported in other literature as well.

4.4 Conclusion

Pure VO₂ particles are produced through thermal decomposition method. The particles annealed at 450 °C have a cluster size of about 1 μm which was composed of particles that have a size distribution between 20~200 nm. The particles were loosely connected and were able to be broken into small particles by 24 hours ball milling process without damaging the crystalline structure. The particles were mixed with PVP and blade cast on a PET film. The thickness of the PVP film was about 300 nm and VO₂(M) particles were well dispersed in the PVP film. The transmittance of the film was little less than 40%, and the IR modulation of about 20% was achieved.

4.5 References

1. Janda, K., *Worldwide status of energy standards for buildings: a 2009 update*. Proceedings of the ECEEE Summer Study, June, 2009: p. 1-6.
2. Li, Y., S. Ji, Y. Gao, H. Luo, and M. Kanehira, *Core-shell VO₂@TiO₂ nanorods that combine thermochromic and photocatalytic properties for application as energy-saving smart coatings*. Scientific reports, 2013. **3**.
3. Blackman, C.S., C. Piccirillo, R. Binions, and I.P. Parkin, *Atmospheric pressure chemical vapour deposition of thermochromic tungsten doped vanadium dioxide thin films for use in architectural glazing*. Thin Solid Films, 2009. **517**(16): p. 4565-4570.
4. Shi, J., S. Zhou, B. You, and L. Wu, *Preparation and thermochromic property of tungsten-doped vanadium dioxide particles*. Solar Energy Materials and Solar Cells, 2007. **91**(19): p. 1856-1862.
5. Xu, C.-l., L. Ma, X. Liu, W.-y. Qiu, and Z.-x. Su, *A novel reduction-hydrolysis method of preparing VO₂ nanopowders*. Materials Research Bulletin, 2004. **39**(7-8): p. 881-886.
6. Bi, A. and J. Zhu, *Hydrothermal synthesis of W and Mo co-doped VO₂ (B) nanobelts*. Journal of Experimental Nanoscience, 2013. **8**(1): p. 46-53.
7. Mwakikunga, B.W., E. Sideras-Haddad, and M. Maaza, *First synthesis of vanadium dioxide by ultrasonic nebula-spray pyrolysis*. Optical Materials, 2007. **29**(5): p. 481-487.
8. Gao, Y., S. Wang, H. Luo, L. Dai, C. Cao, Y. Liu, Z. Chen, and M. Kanehira, *Enhanced chemical stability of VO₂ nanoparticles by the formation of SiO₂/VO₂ core/shell structures and the application to transparent and flexible VO₂-based composite foils with excellent thermochromic properties for solar heat control*. Energy & Environmental Science, 2012. **5**(3): p. 6104-6110.
9. Zhou, J., Y. Gao, X. Liu, Z. Chen, L. Dai, C. Cao, H. Luo, M. Kanahira, C. Sun, and L. Yan, *Mg-doped VO₂ nanoparticles: hydrothermal synthesis, enhanced visible transmittance and decreased metal-insulator transition temperature*. Physical Chemistry Chemical Physics, 2013. **15**(20): p. 7505-7511.

10. Kang, L., Y. Gao, H. Luo, Z. Chen, J. Du, and Z. Zhang, *Nanoporous thermochromic VO₂ films with low optical constants, enhanced luminous transmittance and thermochromic properties*. ACS applied materials & interfaces, 2011. **3**(2): p. 135-138.

Chapter 5. Conclusions and future works

5.1 Summary

Unique properties found in nanostructured materials are different from the same material in bulk form. Many of these properties have huge potential for advanced energy-related technologies. One of the well-recognized superiority of nanostructured material is a very large surface area which is advantageous for heat thermal managing applications. In evaporative cooling, the nanostructured material provides not only the large thermal exchanging surface but also huge capillary force and increased gas-liquid-solid triple contact area. Nanostructure also increases magnetic coercivity of magnetic materials, and alternatively arranged few magnetic domain size of hard phase magnet and soft phase magnet cause strong magnetic exchange coupling between hard phase and soft phase of magnetic materials. In exchanged coupled magnet, the soft phase of magnetic material increase the magnetization of the hard phase magnetic material while slightly decrease coercivity of hard phase magnetic material so that overall $(BH)_{\max}$ increase. Nano-sized materials exhibit unique properties. $\text{VO}_2(\text{M})$ films thicker than ~ 100 nm is constant light absorber. However, the films thinner than ~ 100 nm or particles smaller than ~ 100 nm exhibit IR transmittance modulation functions along metal insulation transition.

In chapter 2 of this dissertation, I discussed our demonstration of evaporative cooling using AAO membrane. Evaporation using ordered nanochannels has several advantages. Many of the previously studied evaporative cooling, liquid supply was maintained through capillary effect by the nano or microstructures on plane direction.

However, nanochannels such as AAO enable the liquid supply cross-plane direction. When liquid is supplied along the plane, liquid often dries out before reaching the center of the heated area. Cross plane direction liquid supply can avoid the liquid dry out . Thus higher heat flux can be achieved. Theoretical calculation shows up to 572 W/cm^2 can be achieved by using AAO membranes that have average pore size 200 nm and thickness of $50 \text{ }\mu\text{m}$. We have successfully demonstrated critical heat flux $\approx 420 \text{ W/cm}^2$ on pore area using IPA. The visualized analysis using speed camera shows that heat flux greater than $\sim 340 \text{ W/cm}^2$ was attributed to evaporation while heat flux lower than $\sim 340 \text{ W/cm}^2$ is due to the combined effect of flooding, boiling and evaporation. The temperature profile shows that membrane temperature was even stable at higher power. Under 80 W/cm^2 , temperature fluctuation is greater than 5 K , however, heat flux higher than $\sim 340 \text{ W/cm}^2$, temperature fluctuation is less than 0.5 K over 80 sec . The temperature even slightly decreased during 80 sec when the critical heat flux was achieved. Relatively low operating temperature is another achievement of this work. Demonstration of most of the evaporative cooling was performed over 100°C which temperature could damage many electrical devices. Operation temperature demonstrated in this work was less than 80°C due to the lower boiling point of IPA compared to water. Our result is further close to the theoretical, critical heat flux value compared to the previous studies. Our demonstration shows that cross plane liquid supply through nanochannels is effective for cooling relatively larger area.

In chapter 3 of this dissertation, I discussed a noble approach to synthesis rare earth free permanent magnet by exchange coupling of hard phase magnetic material and soft phase of the magnetic material. Exchange coupled spring magnet has been

suggested as a promising design to enhance $(BH)_{\max}$ of magnets without rare-earth elements. However, an alternative arrangement of two different phases of magnets in sub-micron or even nanoscale is challenging. Much of demonstration was done by gas phases based depositions such as PVD and CVD. In these approaches, producing even few millimeters thick takes more than few days and is expensive. In our approach, we produced majority volume of hard phase magnetic particles by ball milling of bulk ingot and coated thin layer of soft phase magnet by SAA-PVD process which is designed by our research group. In conventional PVD process, coating materials form a continuous film or solid layer thus the attempt to coat a shell layer on particles would cause agglomeration rather than uniform coating around the particles. Our design of SAPVD process enables constant movement of particles hence agglomeration could be prevented. To demonstrate exchange coupled spring magnet, we have chosen MnBi as a hard phase magnetic material and FeCo as soft phase magnetic material. MnBi particles with a size of 2δ which is about $2\mu\text{m}$ were achieved by ball milling of MnBi ingot 24 hours. After the ball milling process, magnetic remanence of the particles was about 36 emu/g coercivity was about 1.1T. After the SAA-PVD process, magnetic remanence, M_r was increased 51 emu/g and coercivity was decreased to 1T. The $(BH)_{\max}$ of the final product was about 2.5MGOe. EDX element mapping and TEM images show that uniform coating of FeCo layer on the MnBi core. Smooth demagnetization curve and an overall increase of the $(BH)_{\max}$ suggest that exchange coupling of MnBi and FeCo was achieved. We also demonstrated the feasibility of the SAA-PVD process. Adding one more route to produce core-shell structure is worthy since it widens engineering ability to produce noble materials.

In Chapter 4, thermochromic smart window using $\text{VO}_2(\text{M})$ nanoparticles is discussed. $\text{VO}_2(\text{M})$ exhibit fully reversible metal to insulator transition depend on temperature accompanied by a change of optical property. Utilizing this unique optical behavior of the $\text{VO}_2(\text{M})$ enables the control the amount of light entering through windows, thus can save energy. However, the difficulty of producing $\text{VO}_2(\text{M})$ is a high hurdle to overcome before the practical use of $\text{VO}_2(\text{M})$ thermochromic window. Vanadium oxide has a very complex phase system, and $\text{VO}_2(\text{M})$ only forms in very narrow condition. Exploring more routes to produce pure $\text{VO}_2(\text{M})$ is still worthy because of the small yield of most of the $\text{VO}_2(\text{M})$ synthesizing methods. Hydrothermal and gas phase based deposition such as PVD that are currently mostly studied methods.

In this work, we have demonstrated thermal decomposition method to produce $\text{VO}_2(\text{M})$ particles. V_2O_5 was dissolved in liquidus oxalic acid and heated until all liquid evaporated. The dried compound was annealed at 350 °C, 400 °C, 450 °C and 500 °C for 1hour. The particles are ball milled for 24hours and mixed with PVP. After ultrasonic treatment uniform colloidal was achieved, and the mixture was blade cast on PET film. SEM images show that the particles annealed at 450 °C have particle size range between 20~200 nm. Only small portion of particles is out of the range of the optimal size for thermochromic. The fabricated film had about 40% of visible light transmittance and 20% of IR modulation. The demonstrated may need further improvement. The sizes of the particles are not very uniform, and only low energy ball milling process which is slow can be used.

5.2 Future work

Many phenomenon observed on nanomaterial that are dealt in this dissertation are rather complex and requires deeper understanding. As the size of structure approaches nano-regime, either unexpected enhancement or limits emerge that was not able to be foreseen by theoretical modeling. Further systematic studies would enable to elucidate much of key parameters to engineer and design nanostructured materials for energy-related applications.

As discussed in Chapter 2, we have demonstrated critical heat flux much closer to the theoretical works. However, the modeling needs to be verified by much more data points. It is also necessary to study the correlation between critical heat flux and other parameters such as pore size and pore distance and geometry of the pores. The AAO membrane that was used in our demonstration has relatively low thermal conductivity. Membranes with higher thermal conductivity also need to be tested. It was suggested that utilizing thinner membrane would enable heat flux over $5\text{kW}/\text{cm}^2$ [1]. The downside of utilizing a membrane that has a thickness of few micrometers is losing mechanical strength. Hanks et al. designed ridges supported thin membrane and simulated by finite element modeling [2]. In such design, the support can enhance the mechanical strength and provides the microscale liquid supply which promotes capillary force.

In Chapter 3, a demonstration of exchange coupling was discussed. The success of the demonstration was a valuable achievement. However, the $(\text{BH})_{\text{max}}$ value must be much further improved in order to replace the rare earth contained magnets. The

magnetic remanence of our sample was only 36emu/g before SAA-PVD process. If MnBi particles with higher magnetic remanence were used, the overall $(BH)_{\max}$ could be much higher. Previously MnBi particles that have magnetic remanence of 40emu/g and coercivity of 1.0T produced by spark erosion technique was reported [3]. The particles also have spherical shape hence more uniform deposition of FeCo could be done using SAA-PVD process. Another approach to enhance the $(BH)_{\max}$ could be multiple layers of MnBi/FeCo coating using multiple targets and sequenced deposition.

In Chapter 4, a new route to synthesize thermochromic VO_2 particles has discussed. Our result shows that the demonstrated method needs further modification. Slow ball milling process can break the loose connection between each particle without damaging the crystalline structure; the increased process time could be the downside of the low energy ball milling process. Spray pyrolysis could be one of the solutions to eliminate the needs of ball milling process. In spray pyrolysis, the solution is sprayed into heat zone of sealed chamber as a form of mist, and reaction and annealing occur from each single liquid droplet that is hovering in the air thus agglomeration can be avoided [4, 5]. Controlling of the oxygen amount is the key to the success of producing $VO_2(M)$ using spray pyrolysis [6]. There are many studies reported the change of transmittance. However, only a few of the studies measured the change of reflectance response to the phase change of $VO_2(M)$ [7]. More systematic study of reflectance change must be conducted.

5.3 References

1. Xiao, R., S.C. Maroo, and E.N. Wang, *Negative pressures in nanoporous membranes for thin film evaporation*. Applied Physics Letters, 2013. **102**(12): p. 123103.
2. Hanks, D.F., L. Zhengmao, S. Narayanan, K.R. Bagnall, R. Raj, R. Xiao, R. Enright, and E.N. Wang. *Nanoporous evaporative device for advanced electronics thermal management*. in *Thermal and Thermomechanical Phenomena in Electronic Systems (ITherm), 2014 IEEE Intersociety Conference on*. 2014.
3. Nguyen, P.-K., S. Jin, and A.E. Berkowitz, *MnBi particles with high energy density made by spark erosion*. Journal of Applied Physics, 2014. **115**(17): p. 17A756.
4. Pingali, K.C., S. Deng, and D.A. Rockstraw, *Effect of ammonium nitrate on nanoparticle size reduction*. Journal of Nanotechnology, 2008. **2008**.
5. Mančić, L.T., Z.V. Marinković, and O.B. Milošević, *Kinetics of nanocrystalline phase transformations in spray pyrolysed ZnO particles*. Journal of Mining and Metallurgy B: Metallurgy, 2002. **38**(3-4): p. 179-187.
6. Mwakikunga, B.W., E. Sideras-Haddad, and M. Maaza, *First synthesis of vanadium dioxide by ultrasonic nebula-spray pyrolysis*. Optical Materials, 2007. **29**(5): p. 481-487.
7. Gonçalves, A., J. Resende, A.C. Marques, J.V. Pinto, D. Nunes, A. Marie, R. Goncalves, L. Pereira, R. Martins, and E. Fortunato, *Smart optically active VO₂ nanostructured layers applied in roof-type ceramic tiles for energy efficiency*. Solar Energy Materials and Solar Cells, 2016. **150**: p. 1-9.